

Modeling Interactions Between Flexible Flapping-Wing Spars, Mechanisms, and Drive Motors

David B. Doman*

U.S. Air Force Research Laboratory, Wright-Patterson Air Force Base, Ohio 45433-7531

Chin Pei Tang[†]

University of Texas at Dallas, Richardson, Texas 75080-3021

and

Sean Regisford[‡]

U.S. Air Force Research Laboratory, Wright-Patterson Air Force Base, Ohio 45433-7531

DOI: 10.2514/1.53083

A system of dynamical equations is presented that allow micro air vehicle ornithopter designers to match drive motors to loads produced by flexible flapping-wing spars. The model can be used to examine the coupled system-level behavior of brushed dc motors, gear trains, and any number of linkages and flexible wing spars. A Lagrangian approach is used to derive the governing differential equations of motion for a class of ornithopter drive systems. Methods used to determine parametric constants contributing to generalized force components, which cannot be derived from first principles, are described. An example is presented where simulation results are compared with experimental measurements. The results show that the differential equations correctly predict major trends in observed motor speed and wing spar structural deformation over the course of each wingbeat. The results show that when pairing flight-weight motors and wings, significant variations in drive-motor speed occur throughout each wingbeat. It is shown that coupling between motor speed, wing loads, and structural flexibility cause the aerodynamic forces encountered by the wing spars to depart from those predicted by rigid-spar and constant-velocity-motor-based kinematic simulations.

I. Introduction

A LARGE class of micro air vehicle (MAV) ornithopter flapping mechanisms consist of a brushed dc motor and gear train in combination with linkage elements, flexible wing spars, and wing surfaces. The aerodynamic and inertial loads produced by the wings, and the inertial loads produced by gear-train and linkage elements, can significantly affect the instantaneous speed of the motor that drives them. Improperly matched motors and loads can result in repeated starting and stopping of the motor armature, which limits flapping frequency and reduces system performance. Thus, a systematic procedure for modeling the dynamics of this class of electromechanical aeroelastic systems is presented. One potential use for such a model is to serve as the basis for a vehicle design tool that matches drive motors to loads produced by flexible wings. A major objective of this exposition is to present a low-order dynamical model, of adequate fidelity, to predict the characteristics of the motion of flexible wing spars that are driven by ornithopter linkages and brushed dc motors.

There are three principal types of loads that a drive motor must overcome in an ornithopter application, viz., inertial, frictional, and aerodynamic. The inertial loads arise from both rigid-body elements

and flexible modes associated with the structural dynamics of the wings. The frictional loads arise from a combination of viscous and dry friction, where the former is due to light lubricating oils on the gear-train and linkage elements. Additionally, the back-electromotive force, or back-EMF, inherent in all brushed dc motors produces a characteristic that from the point of view of the motor drive torque, behaves like viscous friction.

The Lagrangian method is used to derive a system of governing differential equations that predict the coupled behavior of a brushed dc motor driving a gear train with an arbitrary number of stages, coupled to any number of linkages driving any number of flexible wing spars. Methods for obtaining the generalized forces associated with each degree of freedom are presented for the nonconservative forces and drive elements within the system.

Research in the area of flapping-wing flight has been conducted by both the biological and engineering communities. These communities have leveraged one another's work and it is not uncommon for biologists to make use of aerodynamic theory and theoretical mechanics to characterize and understand the mechanisms that enable flight in insects or birds [1–4]. Likewise, the engineering community has taken advantage of the work of biologists to both devise machines that can approximate the motion of wings observed in nature and to control those motions in such a way as to enable a flapping-wing aircraft to be stabilized and maneuvered as desired. Shyy et al. [5] provide an overview of the work of both communities and provides a foundation for understanding the physics of flapping flight at low Reynolds numbers.

The current state of technology allows one to design and construct ornithopters using ad hoc methods to match loads to motors. A large amount of the work reported in the literature describes the construction of flying prototypes. For instance, the flapping-wing aircraft known as DelFly [6] was developed at Delft University of Technology in The Netherlands and is capable of controlled forward flight and hover. A similar commercially available aircraft, known as the WowWee Dragonfly,[§] is an ornithopter that makes use of four

Presented as Paper 2011-6389 at the 2011 AIAA Guidance, Navigation, and Control Conference, Portland, OR, 8–13 August 2011; received 9 November 2010; revision received 26 April 2011; accepted for publication 29 April 2011. This material is declared a work of the U.S. Government and is not subject to copyright protection in the United States. Copies of this paper may be made for personal or internal use, on condition that the copier pay the \$10.00 per-copy fee to the Copyright Clearance Center, Inc., 222 Rosewood Drive, Danvers, MA 01923; include the code 0731-5090/11 and \$10.00 in correspondence with the CCC.

*Senior Aerospace Engineer, Control Design and Analysis Branch, 2210 Eighth Street, Suite 21; David.Doman@wpafb.af.mil. Associate Fellow AIAA.

[†]Research Associate, Erik Jonsson School of Engineering and Computer Science, 800 West Campbell Road, EC33; Summer Researcher, Control Design and Analysis Branch, U.S. Air Force Research Laboratory, Wright-Patterson Air Force Base, OH 45433-7531; cptang@gmail.com.

[‡]Aerospace Engineer, Control Design and Analysis Branch, 2210 Eighth Street, Suite 21; Sean.Regisford@wpafb.af.mil. Senior Member AIAA.

[§]Data available online at <http://www.wowwee.com/en/products/toys/flight/flytech/dragonfly> [retrieved 8 July 2011].

flapping-wing surfaces to provide propulsion for the aircraft. Researchers at the Naval Postgraduate School developed an aircraft that replaces conventional propulsion mechanisms [7] with flapping wings. Recently, Gerdes et al [8] exhaustively enumerated the flapping-wing aerial vehicles that have had at least one successful reported flight. In a preliminary study [9] on tailless hover-capable ornithopter design, it was found that such aircraft present major challenges associated with trim and control. The work presented here shows the importance of characterizing interactions between loads and drive motors, and the effects that these interactions have upon the aerodynamic forces. It is important for control law designers to be aware of the presence of these interactions and their impact upon the cycle-averaged behavior of the aerodynamic forces and moments.

In terms of designing drive mechanisms for flapping wings, it is desirable to minimize the number of onboard actuators in order to minimize gross takeoff weight. Closed-loop mechanisms such as four-bar linkages have the desirable quality of creating flapping or rocking motion using a single drive actuator. Extensive work has been reported in this area. Researchers have used synthesis-based or optimization-based methods to design mechanisms that *match* the wing motion produced by many flying biological species in a kinematic sense. For instance, the series of designs by Madangopal et al. [10] and McDonald and Agrawal [11] attempted to optimize various mechanism designs, based upon kinematic or quasi-static models of the mechanism motion, in order to match the motion generated by some of the representative flying species. Similarly, Rehmat et al [12] synthesized and fabricated a spherical four-bar mechanism to mimic the figure-eight wing-stroke motion observed in a number of natural flyers. Although they showed simulation and experimental results [13], their proof-of-concept prototype only qualitatively showed the feasibility of such design. Raney and Slominski [14] developed a ground-test apparatus that could vary the wing kinematics produced by a machine that approximated the wing motion observed in hummingbirds. The experiment focused on the control of the wingtip trajectories by varying the amplitude and phase of waveforms applied to two electrodynamic actuators. Chung et al. [15] investigated the use of central pattern generators to control the three dimensional motion of the wings of a 10-degree-of-freedom robotic bat in a wind-tunnel experiment. Other researchers [16–18] have investigated the problem of optimizing wingbeat kinematics for power or aerodynamic efficiency.

In the above efforts, however, the interactions between the drive elements and wing flexibility were not mathematically modeled when optimizing mechanisms for matching the observed motion of natural flyers. In the present exposition, it is shown that the idealized kinematic behavior of a linkage and rigid wing spar driven by a constant velocity dc motor is quite different from that produced by a system where a torque-limited flight-weight motor drives flexible wing spars. As will be shown in the present work, the ability to prescribe wingbeat kinematics in flight-weight systems will not normally be possible because of torque limits and dynamic interactions between drive and wing components. One of the conclusions of the present study is that the entire system, from drive motor to

wing, must be integrated into the model when attempting to match the observed motion of biological systems with a flight-weight mechanical system.

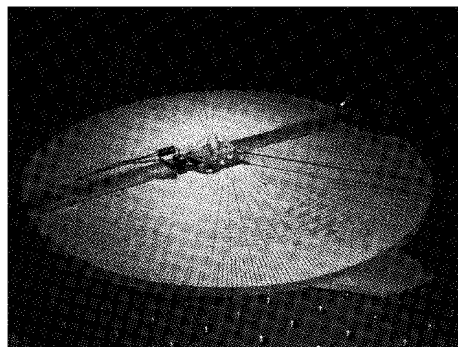
In terms of overall flight control, Deng et al. [19,20] designed, modeled, simulated, and produced a cycle-averaged control design for a conceptual biomimetic flapping-wing robotic aircraft. Khan and Agrawal [21] used a time-averaged control approach in conjunction with a differential flatness based control scheme to design a longitudinal flight controller for a flapping-wing MAV. Dileo and Deng [22] presented a four-wing aircraft design based on a dragonfly that featured a single rotary motor that drove the wings in the stroke plane, a tunable phase difference between the forewings and hind wings using a variable-length coupler link, and passive wing rotation about the spar. In the above control-related studies, the dynamic interactions between the drive components and the flexible and aerodynamic loads were not considered. Because such interactions affect the aerodynamic forces and moments produced by the wings, they will also affect one's ability to control the aircraft.

Finally it is worth noting that there is line of research pursued by Wood et al. [23] that has focused on the development of piezoelectrically powered micromechanical insects. The first takeoff of an insect-scale flapping-wing MAV was achieved by an aircraft called RoboFly that was developed at Harvard University by Wood [24]. Avadhanula et al. [25] modeled a flapping-wing piezoelectrically actuated electromechanical subsystem using a Lagrangian approach. Although piezoelectrically actuated flapping-wing aircraft are an important class of vehicles with a promising future, the work presented here is focused on the fundamentally different dynamic interactions that occur between dc-motor-powered gear trains, linkage-based mechanisms, and flexible wing spars.

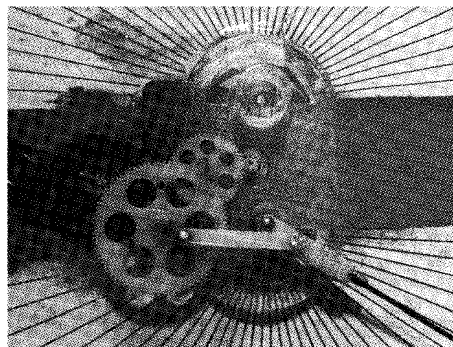
The remainder of the paper is structured as follows: Section II presents a description of the components that comprise the class of systems under consideration. The Lagrangian formalism enables the analysis of the interactions between each subsystem, in terms of energy, and is presented in Sec. III. Section IV evaluates the equation of motion of the system using Lagrange's equation. Taking advantage of the additive properties of derivatives, the equations of motion are derived in a modular fashion. In Sec. V, nonconservative generalized forces, such as drive-motor torque, modal damping, frictional, and aerodynamic forces are derived using the principle of virtual work. The information required to evaluate these terms are supported, in some cases, by experimental measurements. Finally, in Sec. VI, simulation results are critically compared with experimental results generated by the system described in Sec. II.

II. Description of a Bench-Test Article

The framework developed in this paper is directly applicable to a large class of MAV ornithopter designs; however, the simulation and experimental results that are presented, apply to a specific test article that consists of components of a prototype aircraft considered by Doman and Regisford [9]. To introduce the reader to the class of systems under consideration, a specific bench-test article will now be



a) Bench-test article



b) Enlarged view of driving mechanism (diameter of large gear is 2.49 cm)

Fig. 1 Experimental setup.

described. The bench-test article and some of the supporting measurement apparatus is shown in Fig. 1. For the purpose of the analysis in this paper, the system is considered to be rigidly mounted to the bench. The system consists of a coreless brushed dc motor driving a set of compound gears, which in turn drives a four-bar mechanism that imparts rocking motion to a flexible wing spar.

The fuselage frame was produced from a CAD model using a 3-D printer. The gears came from a commercial source. The linkage elements were custom-machined from Delrin. The linkage pins were made from commercially available $\frac{1}{16}$ in. (0.158 cm) aluminum rivets. The spar was made from commercially available 0.037 in. (0.09398 cm) carbon-fiber rod cut to 13 cm in length. The spar was attached to the rocker arm of the linkage using a Kevlar wrap that was saturated with cyanoacrylate adhesive. The fuselage frame also incorporated a custom-made 16-slot optical encoder. The encoder meshed with the linkage crank gear to measure the overall system's angular velocity. Because of the choice of gear ratios, the encoder rotated at the same velocity as the stage 1 gear. The motor power was supplied by a regulated voltage source. A high-speed camera system was used to capture the motion of the system at 2000 frames/second and the images were used to critically compare the motion of the simulation model with that observed in the experiments.

The development that follows applies to a general class of ornithopter flapping mechanisms. The bench-test mechanism described above was used to experimentally validate the equations of motion for a special case.

III. Modeling and Lagrangian Formulation of Each Subsystem

The overall system consists of the following components: a motor, gear train, four-bar linkage, and a flexible wing spar. For the purpose of this paper, the fuselage is assumed to be rigidly mounted to a bench; thus, a fuselage-fixed coordinate frame is taken to be an inertial frame. The motor and the linkage line of centers are also taken to be fixed with respect to the fuselage frame.

In what follows, the kinetic energy T and/or potential energy V of each subsystem is considered. The Lagrangian of a mechanical system is defined as

$$\mathcal{L} \triangleq T - V \quad (1)$$

In the subsequent section, the energy of all of the subsystems are summed together, and the equations of motion of the overall system are determined using Lagrange's equation.

A. DC Motor

First, a model of a brushed dc motor is considered. According to Ogata [26], the torque produced by a motor is proportional to the current flowing through the windings:

$$\tau_\theta = K_T i_a \quad (2)$$

where K_T is the motor torque constant, and i_a is the current. The back-EMF produced by the motor as a result of its angular velocity can be described as

$$e_b = K_b \dot{\theta} \quad (3)$$

where K_b is the back-EMF constant, θ is the angular position of the motor armature, and $\dot{\theta}$ is its angular velocity. The differential equation governing the dynamics of the armature circuit is given by

$$L_a \frac{di_a}{dt} + R_a i_a + e_b = e_a \quad (4)$$

where L_a is the inductance of the motor, R_a is the resistance of the armature, and e_a is the voltage applied to the armature. According to Ogata [26], motor inductance is typically very small; thus, $L_a \approx 0$. Using the small inductance approximation and solving for i_a from Eq. (4) yields

$$i_a = \frac{e_a - e_b}{R_a} \quad (5)$$

Substituting Eqs. (3) and (5) into Eq. (2) allows one to solve for the net torque produced by the motor:

$$\tau_\theta = \frac{K_T}{R_a} e_a - \frac{K_T K_b}{R_a} \dot{\theta} \quad (6)$$

Note that the torque is dependent on the input voltage e_a . The back-EMF and drive torques form a portion of the total generalized force associated with the rigid-body degree of freedom θ .

The rotation of the motor armature contributes kinetic energy to the mechanical system according to

$$T_m = \frac{1}{2} J_a \dot{\theta}^2 \quad (7)$$

where J_a is the mass moment of inertia of the armature and spindle about the axis of rotation. Since the motor does not contribute to the potential energy of the system, the Lagrangian of the *dc motor subsystem* is given by

$$\mathcal{L}_m = T_m = \frac{1}{2} J_a \dot{\theta}^2 \quad (8)$$

B. Gear Train

Many ornithopter designs use compound gear trains to reduce the speed of the motor to achieve a target wing flapping frequency. The overall speed reduction and torque amplification can be tuned, within limits, to match the torque of the motor to the loads produced by the wing and the mechanism.

Figure 2 shows a compound gear train that consists of n_g stages. The stage 0 gear in the train is a pinion fixed to the motor armature. The armature pinion, which has p_0 teeth, meshes with periphery of a first stage compound gear that has t_1 teeth. At each stage, the pinion of each compound gear meshes with the spur gear of the subsequent stage to incrementally increase mechanical advantage and reduce speed until the final crank gear stage n_g is reached. The crank gear stage n_g then forms the crank for the four-bar linkage portion of the drivetrain. The total speed reduction from the pinion to the crank is given by

$$\dot{\theta}_l = \left(\prod_{k=0}^{n_g} G_k \right) \dot{\theta} \quad (9)$$

where $\dot{\theta}_l$ is the crank angular velocity of the four-bar linkage, n_g is the number of gears in the gear train, and G_k is the gear ratio of the k th stage, which for a given gear pitch, is given by

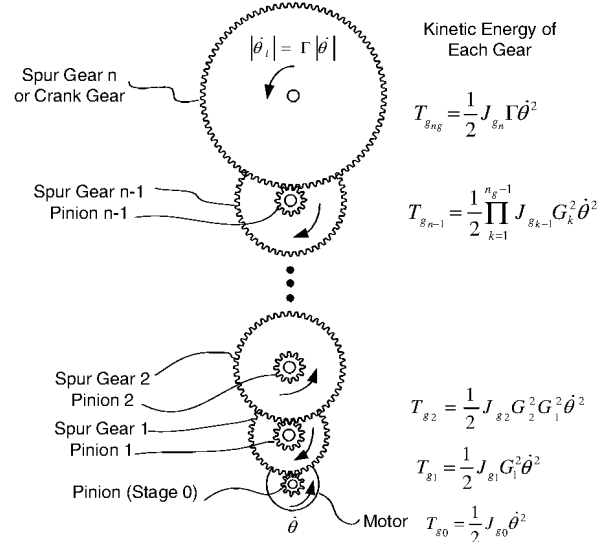


Fig. 2 Compound gear-train transmission.

$$G_k = \begin{cases} 1, & k = 0 \\ \frac{p_{k-1}}{t_k}, & k = 1, 2, \dots \end{cases} \quad (10)$$

where p_{k-1} is the number of teeth on the pinion of compound gear $k-1$, and t_k is the number of teeth on the spur gear k . For convenience, the overall gear ratio from the motor to the crank gear is defined as

$$\Gamma \triangleq \prod_{k=0}^{n_g} G_k \quad (11)$$

Excluding the crank gear, the total kinetic energy and the Lagrangian of the $n_g - 1$ gears and the pinion attached to the motor spindle are given by

$$\mathcal{L}_g = T_g = \frac{1}{2} \left[\sum_{k=0}^{n_g-1} \prod_{j=0}^k J_{gk} G_j^2 \right] \dot{\theta}^2 \quad (12)$$

where J_{g0} is the mass moment of inertia of the pinion, and J_{gk} is the mass moment of inertia of each compound gear in the gear train. Note that the crank gear energy is not included in T_g because it is included in the energy of the linkage that is derived in the subsequent section. Since there is no potential energy contribution from the gear train, the Lagrangian of the *gear-train subsystem* is simply $\mathcal{L}_g = T_g$:

For the system introduced in Sec. II, $n_g = 2$. Hence,

$$\mathcal{L}_g = T_g = \frac{1}{2} (J_{g0} + J_{g1} G_1^2) \dot{\theta}^2 \quad (13)$$

It is worthwhile to note that the kinetic energy of other rotating components, such as encoder wheels used to measure position or speed, can be included by lumping the mass moment of inertia of these components with the mass moment of inertia of any gears that rotate at the same speed. For example, the encoder wheel used in the experiments performed under this work, moves at the same speed as the first stage compound gear. Thus, the effective mass moment of inertia can be computed from the following sum:

$$J'_{g1} \triangleq J_{g1} + J_e + J_{ep} \quad (14)$$

where J_e and J_{ep} represent the mass moments of inertia of the encoder wheel and the pinion attached to the encoder wheel, respectively.

C. Four-Bar Linkage

Figure 3 defines the elements of a four-bar linkage for the class of systems under consideration. The physical structure of the crank gear, viz., gear stage n_g , forms the crank of the four-bar linkage. A pin of mass m_p connects the crank gear to a coupler bar of mass m_2 and mass moment of inertia about its own center of mass of I_2 . The coupler bar is connected to a rocker arm of mass m_3 and mass moment of inertia I_3 by a pin of mass m_p . The line that connects the center of rotation of the crank gear and the pivot point of the rocker arm is called the line of centers, whose length is denoted as l_0 .

Because of the closed-loop kinematic constraints formed within the linkage, the time evolution of the generalized coordinates of the

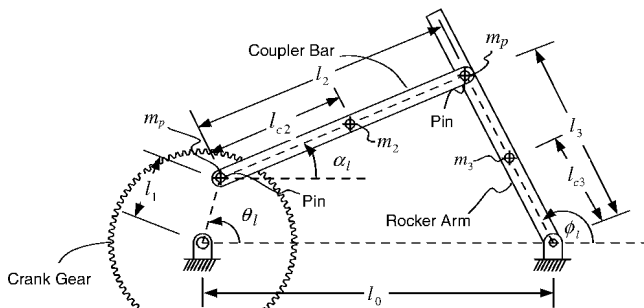


Fig. 3 Four-bar linkage.

crank gear angle θ_1 , coupler angle α_1 , and rocker angle ϕ_1 are highly coupled. However, it is well known that a four-bar linkage is a single-degree-of-freedom system, permitting one to express α_1 and ϕ_1 in terms of θ_1 . Hence, the objective of this section is to establish the total kinetic energy of all the linkage elements in terms of the motor angular velocity $\dot{\theta}$.

1. Four-Bar Linkage Kinematics

To solve the kinematic problem of the four-bar linkage under consideration, the loop-closure constraint equation is written as

$$l_1 \cos \theta_1 + l_2 \cos \alpha_1 = l_0 + l_3 \cos \phi_1 \quad (15)$$

$$l_1 \sin \theta_1 + l_2 \sin \alpha_1 = l_3 \sin \phi_1 \quad (16)$$

Solving for the terms containing α_1 yields

$$l_2 \cos \alpha_1 = l_0 + l_3 \cos \phi_1 - l_1 \cos \theta_1 \quad (17)$$

$$l_2 \sin \alpha_1 = l_3 \sin \phi_1 - l_1 \sin \theta_1 \quad (18)$$

Eliminating α_1 by squaring and summing Eqs. (17) and (18) yields the Freudenstein equation:

$$K_1(\theta_1) \sin \phi_1 + K_2(\theta_1) \cos \phi_1 + K_3(\theta_1) = 0 \quad (19)$$

where

$$K_1(\theta_1) = -2l_1 l_3 \sin \theta_1 \quad (20)$$

$$K_2(\theta_1) = 2l_3(l_0 - l_1 \cos \theta_1) \quad (21)$$

$$K_3(\theta_1) = l_0^2 + l_1^2 - l_2^2 + l_3^2 - 2l_0 l_1 \cos \theta_1 \quad (22)$$

Letting $\tau = \tan(\phi_1/2)$, and making use of double-angle trigonometric identities yields

$$\sin \phi_1 = \frac{2\tau}{1 + \tau^2} \quad (23)$$

$$\cos \phi_1 = \frac{1 - \tau^2}{1 + \tau^2} \quad (24)$$

Substituting Eqs. (23) and (24) into Eq. (19) yields a quadratic equation in τ for a given crank angle θ_1 :

$$(K_3 - K_2)\tau^2 + 2K_1\tau + (K_3 + K_2) = 0 \quad (25)$$

from which one can readily solve for the rocker-arm angle ϕ_1 via

$$\phi_1 = 2 \cdot \arctan 2 \left(\frac{-K_1 \pm \sqrt{K_1^2 - K_3^2 + K_2^2}}{K_3 - K_2} \right) \quad (26)$$

where $\arctan 2$ denotes the four-quadrant arc-tangent function that is dependent upon the signs of the numerator and denominator. The coupler angle α_1 can then be solved by dividing Eq. (17) by Eq. (18):

$$\alpha_1 = \arctan 2 \left(\frac{l_3 \sin \phi_1 - l_1 \sin \theta_1}{l_0 + l_3 \cos \phi_1 - l_1 \cos \theta_1} \right) \quad (27)$$

Hence, $\alpha_1(\theta_1)$ and $\phi_1(\theta_1)$ can effectively be written as functions of θ_1 .

The relationships between the crank angular velocity $\dot{\theta}_1$, and the dependent angular velocities, $\dot{\alpha}_1$ and $\dot{\phi}_1$, can also be determined. Differentiating the loop-closure equations in Eqs. (15) and (16) with respect to time yields

$$-l_1 \dot{\theta}_1 \sin \theta_1 - l_2 \dot{\alpha}_1 \sin \alpha_1 + l_3 \dot{\phi}_1 \sin \phi_1 = 0 \quad (28)$$

$$l_1 \dot{\theta}_1 \cos \theta_1 + l_2 \dot{\alpha}_1 \cos \alpha_1 - l_3 \dot{\phi}_1 \cos \phi_1 = 0 \quad (29)$$

Equations (28) and (29) can be conveniently written as a linear algebra problem that can be solved for $\dot{\alpha}_i$ and $\dot{\phi}_i$ via Cramer's rule, yielding

$$\dot{\alpha}_i = \frac{l_1 \sin(\phi_i - \theta_i)}{l_2 \sin(\alpha_i - \phi_i)} \dot{\theta}_i \quad (30)$$

$$\dot{\phi}_i = \frac{l_1 \sin(\alpha_i - \theta_i)}{l_3 \sin(\alpha_i - \phi_i)} \dot{\theta}_i \quad (31)$$

Since $\theta_i = \Gamma\theta$, Eqs. (30) and (31) can be written as

$$\dot{\alpha}_i = S_1(\theta)\dot{\theta} = \frac{\partial \alpha_i}{\partial \theta} \dot{\theta} \quad (32)$$

$$\dot{\phi}_i = S_2(\theta)\dot{\theta} = \frac{\partial \phi_i}{\partial \theta} \dot{\theta} \quad (33)$$

where

$$S_1(\theta) \triangleq \Gamma \frac{l_1 \sin(\phi_i - \Gamma\theta)}{l_2 \sin(\alpha_i - \phi_i)} \quad (34)$$

$$S_2(\theta) \triangleq \Gamma \frac{l_1 \sin(\alpha_i - \Gamma\theta)}{l_3 \sin(\alpha_i - \phi_i)} \quad (35)$$

Therefore, the linkage element velocities $\dot{\alpha}_i$, $\dot{\phi}_i$, and $\dot{\theta}_i$ can be written in terms of a single motion variable and its time derivative, viz., the motor angular position θ and angular velocity $\dot{\theta}$.

2. Lagrangian of Four-Bar Linkage

The kinetic energy of the linkage elements is given by

$$T_l = \frac{1}{2}m_1 \|v_{c_1}\|^2 + I_1 \dot{\theta}_1^2 + m_2 \|v_{c_2}\|^2 + I_2 \dot{\alpha}_1^2 + m_3 \|v_{c_3}\|^2 + I_3 \dot{\phi}_1^2 + m_p (\|v_{p_1}\|^2 + \|v_{p_2}\|^2) \quad (36)$$

where v_{c_1} , v_{c_2} and v_{c_3} are the linear velocities of the centers of mass of the crank, coupler, and rocker, respectively; m_p is the mass of the linkage pins; and v_{p_1} and v_{p_2} are the velocities of the two pins. The center of mass of the crank is constant because it is formed from the final gear, which is axisymmetric; thus, $v_{c_1} = 0$ and $I_1 = J_{gns}$. Expanding Eq. (36) yields

$$T_l = \frac{1}{2}I_1 \dot{\theta}_1^2 + m_2 (l_1^2 \dot{\theta}_1^2 + l_2^2 \dot{\alpha}_1^2 + 2l_1 l_2 \cos(\theta_1 - \alpha_1) \dot{\alpha}_1 \dot{\theta}_1) + I_2 \dot{\alpha}_1^2 + (m_3 l_3^2 + I_3) \dot{\phi}_1^2 + m_p (l_1^2 \dot{\theta}_1^2 + l_3^2 \dot{\phi}_1^2) \quad (37)$$

Collecting terms on the products of the angular velocities and substituting Eqs. (9) and (11) into Eq. (37) yields

$$T_l = \frac{1}{2}[J_1 \dot{\theta}^2 + J_2 \dot{\alpha}_1^2 + J_3 \dot{\phi}_1^2 + 2P_1 C_1 \dot{\alpha}_1 \dot{\theta}] \quad (38)$$

where

$$J_1 = \Gamma^2 [I_1 + m_2 l_1^2 + m_p l_1^2] \quad (39)$$

$$J_2 = m_2 l_2^2 + I_2 \quad (40)$$

$$J_3 = m_3 l_3^2 + m_p l_3^2 + I_3 \quad (41)$$

$$P_1 = m_2 l_1 l_2 \Gamma \quad (42)$$

$$C_1 = \cos(\theta_i - \alpha_i) \quad (43)$$

Note that the linkage operates in a plane that is perpendicular to the gravitational vector; thus, there is no change in potential energy of the linkage elements as the crank rotates. Hence, only kinetic energy contributes to the total Lagrangian associated with the *four-bar*

linkage subsystem. Substituting Eqs. (30) and (31) into Eq. (38) yields the complete expression for the kinetic energy and Lagrangian of the linkage in terms of the motor angular velocity $\dot{\theta}$:

$$\mathcal{L}_l = T_l = \frac{1}{2}[J_1 \dot{\theta} + J_2 S_1^2 + J_3 S_2^2 + 2P_1 C_1 S_1] \dot{\theta}^2 \quad (44)$$

D. Flexible Spar

Typical MAV ornithopters use carbon-fiber components for the wing structure and thin films, such as Mylar, for the wing skin. In general, the interactions of the motor, gears, linkage, and wing are of interest. In the analysis that follows, the structural dynamics of a wing spar are considered, since the leading-edge wing spar provides the primary resistance to wing bending in the stroke plane. Figure 4 shows a diagram of a four-bar linkage with a flexible wing spar clamped to the end of a rocker arm.

An inertial frame, represented by the unit vectors \hat{n}_1, \hat{n}_2 , is fixed at the center of rotation of the rocker arm. A coordinate frame that rotates with the rocker arm is denoted as \hat{s}_1, \hat{s}_2 . A vector from the origin of frame $\hat{s}_1 - \hat{s}_2$ to the point at which the spar is clamped to the rocker arm is denoted as \mathbf{r}_r . A vector from the clamped root of the spar to an arbitrary point on the undeformed spar is denoted as \mathbf{r}_u . A vector from a point on the undeformed spar to a point on the deformed spar is denoted as $w(r_u, t)$ where $r_u \triangleq \|\mathbf{r}_u\|$. The deformation $w(r_u, t)$ is taken to be perpendicular to the undeformed spar and therefore occurs only in the \hat{s}_2 direction. When viewed from the rocker-arm frame, the flexible spar appears as a cantilever beam. (Note that the rocker-arm angle ϕ_i remains a function of motor position θ .) The motion of the rocker arm will cause the spar to deform due to bending. Euler-Bernoulli beam theory is used in the following analysis and the spar is taken to have uniform cross section and Young's modulus. The assumed modes method [27] is used to describe the deformation of the spar in the stroke plane relative to the \hat{s}_1 axis. The deformation is taken to be described by an infinite sum of the products of spatially dependent mode shape functions $\Phi_i(r_u)$ and temporal modal coordinates $\eta_i(t)$, i.e.,

$$w(r_u, t) = \sum_{i=1}^{\infty} \Phi_i(r_u) \eta_i(t) \quad (45)$$

where for clamped-free boundary conditions, the i th mode shape function is given by

$$\Phi_i(r_u) = A_i [a_i (\sin \beta_i r_u - \sinh \beta_i r_u) + b_i (\cos \beta_i r_u - \cosh \beta_i r_u)] \quad (46)$$

where

$$a_i \triangleq (\sin \beta_i L - \sinh \beta_i L) \quad (47)$$

$$b_i \triangleq (\cos \beta_i L + \cosh \beta_i L) \quad (48)$$

and β_i is the i th solution to the frequency equation,

$$\cos \beta_i L \cosh \beta_i L = -1 \quad (49)$$

and A_i is an arbitrary constant with units of length. In the literature, the arbitrary constant associated with each mode is often used to mass-normalize the mode shapes.

For a cantilever beam with uniform properties along its length,

$$\beta_i^4 = \frac{\omega_i^2 \hat{m}}{E_s I_s} \quad (50)$$

where ω_i is the natural frequency of the i th bending mode, \hat{m} is the mass per unit length of the beam, E_s is the Young's modulus of the spar, and I_s is the area moment of inertia of the cross section of the spar about the neutral axis.

In the analysis that follows, the *first and second bending modes* are retained in the response.[†] Hence,

$$w(r_u, t) = \Phi_1(r_u)\eta_1(t) + \Phi_2(r_u)\eta_2(t) \quad (51)$$

Solving the frequency equation for the first two bending modes yields

$$\omega_1 = 1.875^2 \sqrt{\frac{E_s I_s}{\hat{m} L^4}} \quad (52)$$

$$\omega_2 = 4.694^2 \sqrt{\frac{E_s I_s}{\hat{m} L^4}} \quad (53)$$

where the constants are accurate to four significant figures. It is also useful to note that

$$\beta_1 = \frac{1.875}{L} \quad (54)$$

$$\beta_2 = \frac{4.694}{L} \quad (55)$$

1. Flexible-Spar Kinetic Energy

For convenience, define $r \triangleq r_r + r_u$. Note that r_r extends along the rigid rocker arm from the pivot point to the clamped end of the spar. From Fig. 4, one may write the position vector from the origin of the rocker arm to a point on the deformed beam as

$$\mathbf{r}_p = [r \cos \phi_i - w \sin \phi_i] \hat{n}_1 + [r \sin \phi_i + w \cos \phi_i] \hat{n}_2 \quad (56)$$

Substituting Eq. (51) yields

$$\begin{aligned} \mathbf{r}_p = & [r \cos \phi_i - (\Phi_1 \eta_1 + \Phi_2 \eta_2) \sin \phi_i] \hat{n}_1 \\ & + [r \sin \phi_i + (\Phi_1 \eta_1 + \Phi_2 \eta_2) \cos \phi_i] \hat{n}_2 \end{aligned} \quad (57)$$

Differentiating Eq. (57) with respect to time yields

$$\begin{aligned} \dot{\mathbf{r}}_p = & [-r \dot{\phi}_i \sin \phi_i - (\Phi_1 \eta_1 + \Phi_2 \eta_2) \dot{\phi}_i \cos \phi_i \\ & - (\Phi_1 \dot{\eta}_1 + \Phi_2 \dot{\eta}_2) \sin \phi_i] \hat{n}_1 + [r \dot{\phi}_i \cos \phi_i \\ & - (\Phi_1 \eta_1 + \Phi_2 \eta_2) \dot{\phi}_i \sin \phi_i + (\Phi_1 \dot{\eta}_1 + \Phi_2 \dot{\eta}_2) \cos \phi_i] \hat{n}_2 \end{aligned} \quad (58)$$

The differential kinetic energy of an elemental beam segment on the deformable spar is given by

$$dT_s = \frac{1}{2} \hat{m} [\dot{\mathbf{r}}_p \cdot \dot{\mathbf{r}}_p] dr \quad (59)$$

or, with some mathematical manipulation,

$$\begin{aligned} dT_s = & \frac{1}{2} \hat{m} [r^2 \dot{\phi}_i^2 + (\Phi_1 \eta_1 + \Phi_2 \eta_2)^2 \dot{\phi}_i^2 + (\Phi_1 \dot{\eta}_1 + \Phi_2 \dot{\eta}_2)^2 \\ & + 2r \dot{\phi}_i (\Phi_1 \dot{\eta}_1 + \Phi_2 \dot{\eta}_2)] dr \end{aligned} \quad (60)$$

Integrating Eq. (60) from the root to the tip of the spar yields

$$\begin{aligned} T_s = & \frac{1}{2} \hat{m} \int_{r_r}^{r_r+L} [r^2 \dot{\phi}_i^2 + (\Phi_1 \eta_1 + \Phi_2 \eta_2)^2 \dot{\phi}_i^2 + (\Phi_1 \dot{\eta}_1 + \Phi_2 \dot{\eta}_2)^2 \\ & + 2r \dot{\phi}_i (\Phi_1 \dot{\eta}_1 + \Phi_2 \dot{\eta}_2)] dr \end{aligned} \quad (61)$$

or

$$\begin{aligned} T_s = & \frac{1}{2} \hat{m} \int_0^L [(r_r + r_u)^2 \dot{\phi}_i^2 + (\Phi_1 \eta_1 + \Phi_2 \eta_2)^2 \dot{\phi}_i^2 + (\Phi_1 \dot{\eta}_1 \\ & + \Phi_2 \dot{\eta}_2)^2 + 2(r_r + r_u) \dot{\phi}_i (\Phi_1 \dot{\eta}_1 + \Phi_2 \dot{\eta}_2)] dr_u \end{aligned} \quad (62)$$

[†]For the case considered in the Results section, it was found that retaining only the first bending mode yielded excellent results; nevertheless, a more general two-mode case has been considered in the analytical development.

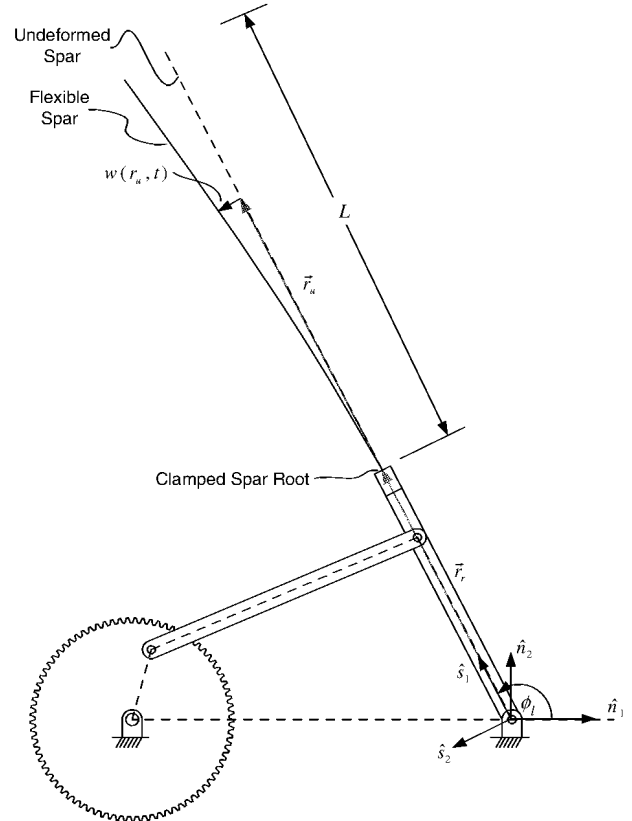


Fig. 4 Flexible spar driven by rocker arm.

Recall that the shape functions, Φ_i , are functions of r_u only, and that ϕ_i, η_1 and η_2 are functions of time and do not vary with r_u . Carrying out the integration of Eq. (62) yields

$$\begin{aligned} T_s = & \frac{1}{2} \hat{m} [c_1 \dot{\phi}_i^2 + c_2 (\dot{\phi}_i^2 \eta_1^2 + \dot{\eta}_1^2) + 2c_4 \dot{\phi}_i \dot{\eta}_1 + 2c_6 (\eta_1 \eta_2 \dot{\phi}_i^2 + \dot{\eta}_1 \dot{\eta}_2) \\ & + c_7 (\dot{\phi}_i^2 \eta_2^2 + \dot{\eta}_2^2) + 2c_8 \dot{\phi}_i \dot{\eta}_2] \end{aligned} \quad (63)$$

where

$$c_1 = \int_0^L (r_r + r_u)^2 dr_u = \frac{L^3}{3} + L^2 r_r + L r_r^2 \quad (64)$$

$$c_2 = \int_0^L \Phi_1^2 dr_u = 9.226L \quad (65)$$

$$c_4 = \int_0^L (r_r + r_u) \Phi_1 dr_u = -L(1.728L + 2.378r_r) \quad (66)$$

$$c_6 = \int_0^L \Phi_1 \Phi_2 dr_u = 0 \quad (67)$$

$$c_7 = \int_0^L \Phi_2^2 dr_u = 2984.480L \quad (68)$$

$$c_8 = \int_0^L (r_r + r_u) \Phi_2 dr_u = -L(4.959L + 23.707r_r) \quad (69)$$

Note that the decimal constants in c_2 and c_7 have units of length squared, while the decimal constants in c_4 and c_8 have units of length, and c_6 is 0, since the mode shapes are orthogonal. Substituting Eqs. (35) and (67) into Eq. (63) yields

$$\begin{aligned} T_s = & \frac{1}{2} \hat{m} [c_1 S_2^2 \dot{\theta}^2 + c_2 (S_2^2 \dot{\theta}^2 \eta_1^2 + \dot{\eta}_1^2) + 2c_4 S_2 \dot{\theta} \dot{\eta}_1 \\ & + c_7 (S_2^2 \dot{\theta}^2 \eta_2^2 + \dot{\eta}_2^2) + 2c_8 S_2 \dot{\theta} \dot{\eta}_2] \end{aligned} \quad (70)$$

The kinetic energy of the spar is now written in terms of the three motion variables of interest, viz., θ , η_1 , and η_2 and their derivatives.

2. Flexible-Spar Strain Energy

By definition, the strain energy due to bending of an Euler-Bernoulli beam is given by [28]

$$V_s = \frac{1}{2} E_s I_s \int_0^L w''(r_u, t)^2 dr_u \quad (71)$$

Retaining only the first two bending modes and setting the arbitrary constant A_i of Eq. (46) to unity, the second spatial derivative of the deformation becomes

$$\begin{aligned} w''(r_u, t) = & \beta_1^2 [-a_1 (\cos \beta_1 r_u + \cosh \beta_1 r_u) - b_1 (\sin \beta_1 r_u \\ & + \sinh \beta_1 r_u)] \eta_1 + \beta_2^2 [-a_2 (\cos \beta_2 r_u + \cosh \beta_2 r_u) \\ & - b_2 (\sin \beta_2 r_u + \sinh \beta_2 r_u)] \eta_2 \end{aligned} \quad (72)$$

Squaring Eq. (72) and evaluating Eq. (71) yields the strain energy of the spar due to bending deformation from the first two bending modes:

$$V_s = \frac{1}{2} E_s I_s [c_5 \eta_1^2 + c_{10} \eta_2^2] \quad (73)$$

where

$$c_5 = \int_0^L \Phi_1^{2''} dr_u = \frac{114.082}{L^3} \quad (74)$$

$$c_{10} = \int_0^L \Phi_2^{2''} dr_u = \frac{1.449 \times 10^6}{L^3} \quad (75)$$

Integrals of the products of the two mode shapes are zero because of orthogonality. The decimal constants in c_5 and c_{10} have units of length squared. The contribution of the flexible-spar subsystem to the Lagrangian is

$$\mathcal{L}_s = T_s - V_s \quad (76)$$

or

$$\begin{aligned} \mathcal{L}_s = & \frac{1}{2} \hat{m} [c_1 \dot{S}_2^2 \hat{\theta}^2 + c_2 (S_2^2 \hat{\theta}^2 \eta_1^2 + \dot{\eta}_1^2) + 2c_4 S_2 \hat{\theta} \dot{\eta}_1 \\ & + c_7 (S_2^2 \hat{\theta}^2 \eta_2^2 + \dot{\eta}_2^2) + 2c_8 S_2 \hat{\theta} \dot{\eta}_2] - E_s I_s [c_5 \eta_1^2 + c_{10} \eta_2^2] \end{aligned} \quad (77)$$

IV. Equations of Motion

In Sec. III, the Lagrangian contribution of each subsystem was evaluated. The full equations of motion can now be derived using Lagrange's equation:

$$\frac{d}{dt} \left(\frac{\partial \mathcal{L}}{\partial \dot{q}_i} \right) - \frac{\partial \mathcal{L}}{\partial q_i} = Q \quad (78)$$

where q_i represents the i th generalized displacement coordinate, and Q_i the corresponding generalized forces derived from the principle of virtual work.

For the system under consideration, there are three generalized coordinates: namely, θ , η_1 , and η_2 . Hence, three coupled ordinary differential equations of motion are derived. The Lagrangian of the entire system can be obtained by summing Eqs. (8), (12), (44), and (77):

$$\mathcal{L} = \mathcal{L}_m + \mathcal{L}_g + \mathcal{L}_l + \mathcal{L}_s \quad (79)$$

Although this paper studies a system where a dc motor drives a single gear train and four-bar linkage assembled with a flexible spar attached to the rocker arm, it is straightforward to extend the formulation to account for systems with additional elements. For instance, it is common for ornithopters to use a single motor to drive two linkage-spar assemblies, as presented by Doman and Regisford

[9], or a single linkage assembly to drive two spars. For such cases, let n_l be the number of linkage assemblies and let n_s be the number of spars attached to the linkages. Assuming that only identical copies of such elements are added to the system, the more general Lagrangian can be written as

$$\mathcal{L} = \mathcal{L}_m + \mathcal{L}_g + n_l \mathcal{L}_l + n_s \mathcal{L}_s \quad (80)$$

The remainder of this section evaluates the inertial and Coriolis/centrifugal terms associated with the left-hand side of Lagrange's equation in Eq. (78). In the interest of establishing a general set of equations in which components may be added or subtracted from the system, we note that the derivative of a sum is equal to the sum of the derivatives; thus Lagrange's equation can be evaluated for each component, and the results can be added together to create the full equations of motion. One can derive the more general cases using the Lagrangian shown in Eq. (80).

A. DC Motor

Referring to Eq. (8), it can be seen that the Lagrangian associated with the motor is a function of the single motion variable $\hat{\theta}$. Hence, it is straightforward to show that the contribution of the motor to the equation of motion associated with the rigid-body degree of freedom is given by

$$\frac{d}{dt} \left(\frac{\partial \mathcal{L}_m}{\partial \dot{\hat{\theta}}} \right) = J_a \ddot{\hat{\theta}} \quad (81)$$

The motor also contributes to the nonconservative input torque:

$$Q_{m\theta} = \tau_\theta \quad (82)$$

Recall that τ_θ includes the effects of the voltage applied to the armature and the back-EMF damping effect, which is a function of the motion variable $\hat{\theta}$.

B. Gear Train

The Lagrangian expression for the gear train in Eq. (12), is a function of $\hat{\theta}$ only. Hence, the contribution of the gear train to the equation of motion of motion associated with the rigid-body degree of freedom can be evaluated as

$$\frac{d}{dt} \left(\frac{\partial \mathcal{L}_g}{\partial \dot{\hat{\theta}}} \right) = \left(\sum_{k=0}^{n_g-1} \prod_{j=1}^k J_{gk} G_j^2 \right) \ddot{\hat{\theta}} \quad (83)$$

For the test article considered in this paper, Eq. (13) yields

$$\frac{d}{dt} \left(\frac{\partial \mathcal{L}_g}{\partial \dot{\hat{\theta}}} \right) = J_{g\theta} \ddot{\hat{\theta}} \quad (84)$$

where

$$J_{g\theta} = (J_{g0} + J'_{g1} G_1^2) \quad (85)$$

in which the mass moment of inertia of the encoder is also included.

C. Four-Bar Linkage

The Lagrangian of the four-bar linkage \mathcal{L}_l is completely written in terms of θ and $\dot{\theta}$ as shown in Eq. (44); however, due to the highly nonlinear couplings between the angular quantities, care must be taken to ensure that all dependencies are considered when evaluating the derivatives associated with Lagrange's equation. The contribution of the four-bar linkage to the equation of motion associated with the rigid-body degree of freedom is given by

$$\frac{d}{dt} \left(\frac{\partial \mathcal{L}_l}{\partial \dot{\theta}} \right) - \frac{\partial \mathcal{L}_l}{\partial \theta} \quad (86)$$

Examination of Eqs. (34), (35), and (38) reveals that S_1 , S_2 , and C_1 are functions of all of the angular position variables associated with

the four-bar linkage, which can be expressed in terms of the time-dependent motor angular position: i.e.,

$$S_1(\theta(t), \alpha_i(\theta(t)), \phi_i(\theta(t))), \quad S_2(\theta(t), \alpha_i(\theta(t)), \phi_i(\theta(t))) \\ C_1(\theta(t), \alpha_i(\theta(t))) \quad (87)$$

For brevity, in the subsequent development the dependence of these terms upon $\theta(t)$ is implied rather than explicitly written. To evaluate Eq. (86), it is necessary to compute the time derivatives of these functions. Application of the multivariable chain rule yields

$$\frac{dS_1}{dt} = \tilde{S}_1 \frac{d\theta}{dt} \quad (88)$$

$$\frac{dS_2}{dt} = \tilde{S}_2 \frac{d\theta}{dt} \quad (89)$$

$$\frac{dC_1}{dt} = \tilde{C}_1 \frac{d\theta}{dt} \quad (90)$$

where

$$\tilde{S}_1 = \left[\frac{\partial S_1}{\partial \theta} + \frac{\partial S_1}{\partial \alpha_i} \frac{\partial \alpha_i}{\partial \theta} + \frac{\partial S_1}{\partial \phi_i} \frac{\partial \phi_i}{\partial \theta} \right] \quad (91)$$

$$\tilde{S}_2 = \left[\frac{\partial S_2}{\partial \theta} + \frac{\partial S_2}{\partial \alpha_i} \frac{\partial \alpha_i}{\partial \theta} + \frac{\partial S_2}{\partial \phi_i} \frac{\partial \phi_i}{\partial \theta} \right] \quad (92)$$

$$\tilde{C}_1 = \left[\frac{\partial C_1}{\partial \theta} + \frac{\partial C_1}{\partial \alpha_i} \frac{\partial \alpha_i}{\partial \theta} \right] \quad (93)$$

However, from Eqs. (34) and (35), it readily follows that

$$\tilde{S}_1 = \left[\frac{\partial S_1}{\partial \theta} + \frac{\partial S_1}{\partial \alpha_i} S_1 + \frac{\partial S_1}{\partial \phi_i} S_2 \right] \quad (94)$$

$$\tilde{S}_2 = \left[\frac{\partial S_2}{\partial \theta} + \frac{\partial S_2}{\partial \alpha_i} S_1 + \frac{\partial S_2}{\partial \phi_i} S_2 \right] \quad (95)$$

$$\tilde{C}_1 = \left[\frac{\partial C_1}{\partial \theta} + \frac{\partial C_1}{\partial \alpha_i} S_1 \right] \quad (96)$$

where the full expressions for the individual partial derivatives can be found in the Appendix. Hence, evaluating each of the terms in Eq. (86) yields

$$\frac{d}{dt} \left(\frac{\partial \mathcal{L}_l}{\partial \dot{\theta}} \right) = J_{i_\theta} \ddot{\theta} + 2\sigma_{i_\theta} \dot{\theta}^2 \quad (97)$$

$$\frac{\partial \mathcal{L}_l}{\partial \theta} = \sigma_{i_\theta} \dot{\theta}^2 \quad (98)$$

where

$$J_{i_\theta} = J_{1_i} + J_{2_i} S_1^2 + J_{3_i} S_2^2 + 2P_1 C_1 S_1 \quad (99)$$

$$\sigma_{i_\theta} = (P_1 C_1 + J_{2_i} S_1) \tilde{S}_1 + J_{3_i} S_2 \tilde{S}_2 + P_1 S_1 \tilde{C}_1 \quad (100)$$

Finally, Eq. (86) becomes

$$\frac{d}{dt} \left(\frac{\partial \mathcal{L}_l}{\partial \dot{\theta}} \right) - \frac{\partial \mathcal{L}_l}{\partial \theta} = J_{i_\theta} \ddot{\theta} + \sigma_{i_\theta} \dot{\theta}^2 \quad (101)$$

D. Flexible Spar

For the Lagrangian of the flexible spar in Eq. (77), note that all three generalized coordinates, θ , η_1 and η_2 , are involved. Hence, the flexible spar will contribute to three equations of motion. Evaluation of Lagrange's equation for the coordinate θ yields

$$\frac{d}{dt} \left(\frac{\partial \mathcal{L}_s}{\partial \dot{\theta}} \right) - \frac{\partial \mathcal{L}_s}{\partial \theta} = J_{s_\theta}^\theta \ddot{\theta} + J_{s_\theta}^{\eta_1} \ddot{\eta}_1 + J_{s_\theta}^{\eta_2} \ddot{\eta}_2 + \sigma_{s_\theta} \dot{\theta}^2 + \kappa_{s_\theta} \quad (102)$$

where

$$J_{s_\theta}^\theta = \hat{m} S_2^2 (c_1 + c_2 \eta_1^2 + c_7 \eta_2^2) \quad (103)$$

$$J_{s_\theta}^{\eta_1} = \hat{m} c_4 S_2 \quad (104)$$

$$J_{s_\theta}^{\eta_2} = \hat{m} c_8 S_2 \quad (105)$$

$$\sigma_{s_\theta} = \hat{m} S_2 \tilde{S}_2 (c_1 + c_2 \eta_1^2 + c_7 \eta_2^2) \quad (106)$$

$$\kappa_{s_\theta} = 2\hat{m} S_2^2 \dot{\theta} (c_2 \dot{\eta}_1 \eta_1 + c_7 \dot{\eta}_2 \eta_2) \quad (107)$$

Evaluation of Lagrange's equation for the coordinate η_1 yields

$$\frac{d}{dt} \left(\frac{\partial \mathcal{L}_s}{\partial \dot{\eta}_1} \right) - \frac{\partial \mathcal{L}_s}{\partial \eta_1} = J_{s_{\eta_1}}^\theta \ddot{\theta} + J_{s_{\eta_1}}^{\eta_1} \ddot{\eta}_1 + \sigma_{s_{\eta_1}} \dot{\theta}^2 + \kappa_{s_{\eta_1}} \quad (108)$$

where

$$J_{s_{\eta_1}}^\theta = \hat{m} c_4 S_2 \quad (109)$$

$$J_{s_{\eta_1}}^{\eta_1} = \hat{m} c_2 \quad (110)$$

$$\sigma_{s_{\eta_1}} = \hat{m} (c_4 \tilde{S}_2 - c_2 S_2^2 \eta_1) \quad (111)$$

$$\kappa_{s_{\eta_1}} = E_s I_s c_5 \eta_1 \quad (112)$$

Evaluation of Lagrange's equation for the coordinate η_2 yields

$$\frac{d}{dt} \left(\frac{\partial \mathcal{L}_s}{\partial \dot{\eta}_2} \right) - \frac{\partial \mathcal{L}_s}{\partial \eta_2} = J_{s_{\eta_2}}^\theta \ddot{\theta} + J_{s_{\eta_2}}^{\eta_2} \ddot{\eta}_2 + \sigma_{s_{\eta_2}} \dot{\theta}^2 + \kappa_{s_{\eta_2}} \quad (113)$$

where

$$J_{s_{\eta_2}}^\theta = \hat{m} c_8 S_2 \quad (114)$$

$$J_{s_{\eta_2}}^{\eta_2} = \hat{m} c_7 \quad (115)$$

$$\sigma_{s_{\eta_2}} = \hat{m} (c_8 \tilde{S}_2 - c_7 S_2^2 \eta_2) \quad (116)$$

$$\kappa_{s_{\eta_2}} = E_s I_s c_{10} \eta_2 \quad (117)$$

E. Complete Equations of Motion

Finally, the complete equations of motion can be written as

$$\begin{bmatrix} J_a + J_{g_\theta} + J_{i_\theta}(\theta) + J_{s_\theta}^\theta(\theta) & J_{s_\theta}^{\eta_1}(\theta) & J_{s_\theta}^{\eta_2}(\theta) \\ J_{s_{\eta_1}}^\theta(\theta) & J_{s_{\eta_1}}^{\eta_1} & 0 \\ J_{s_{\eta_2}}^\theta(\theta) & 0 & J_{s_{\eta_2}}^{\eta_2} \end{bmatrix} \begin{bmatrix} \ddot{\theta} \\ \ddot{\eta}_1 \\ \ddot{\eta}_2 \end{bmatrix} \\ + \begin{bmatrix} \sigma_{i_\theta}(\theta) + \sigma_{s_\theta}(\theta, \eta_1, \eta_2) \\ \sigma_{s_{\eta_1}}(\theta, \eta_1) \\ \sigma_{s_{\eta_2}}(\theta, \eta_2) \end{bmatrix} \dot{\theta}^2 + \begin{bmatrix} \kappa_{s_\theta}(\theta, \dot{\theta}, \eta_1, \dot{\eta}_1, \eta_2, \dot{\eta}_2) \\ \kappa_{s_{\eta_1}}(\eta_1) \\ \kappa_{s_{\eta_2}}(\eta_2) \end{bmatrix} \\ = \begin{bmatrix} Q_{m_\theta}(e_a) + Q_{i_\theta}(\dot{\theta}) + Q_{d_\theta}(\theta, \dot{\theta}, \eta_1, \dot{\eta}_1, \eta_2, \dot{\eta}_2) \\ Q_{s_{\eta_1}}(\dot{\eta}_1) + Q_{d_{\eta_1}}(\theta, \dot{\theta}, \eta_1, \dot{\eta}_1, \eta_2, \dot{\eta}_2) \\ Q_{s_{\eta_2}}(\dot{\eta}_2) + Q_{d_{\eta_2}}(\theta, \dot{\theta}, \eta_1, \dot{\eta}_1, \eta_2, \dot{\eta}_2) \end{bmatrix} \quad (118)$$

which can be integrated using numerical methods. The explicit dependence of the inertial, Coriolis, and generalized force terms upon the state variables is shown to highlight the extensive coupling present in such a system. The forcing term that drives these equations is the armature voltage e_a . Thus, these equations can be used to predict how the system will behave when a constant or time-varying voltage is applied to the motor armature. These equations provide a powerful analysis tool for MAV system designers. They could also be used as a model to support the design of mechanism control laws that have the potential to improve the behavior of wing beat motion over what could be achieved by applying a constant voltage to the motor.

There are a number of generalized forces that act upon the system such as a velocity-dependent frictional/back-EMF term associated with the θ coordinate, which can be written as $Q_{i_\theta} = B_\theta \dot{\theta}$; the damping within the flexible spar that is proportional to the modal coordinate rates $Q_{s_{\eta_1}} = 2\zeta_1 \omega_1 \dot{\eta}_1$ and $Q_{s_{\eta_2}} = 2\zeta_2 \omega_2 \dot{\eta}_2$; and the aerodynamic drag of the spar that influences each degree of freedom via Q_{d_θ} , $Q_{d_{\eta_1}}$, and $Q_{d_{\eta_2}}$. Methods for estimating each of these generalized forces will be discussed in the next two sections.

V. Estimation of Generalized Forces

The analytical method presented thus far yields the form of the governing dynamical equations. There are several constants that are device-dependent and can only be determined experimentally. With respect to the dc motor, the motor torque constant K_T , back-EMF constant K_b , and armature resistance R_a must be determined experimentally or be provided by the motor manufacturer. The friction characteristics of the gear train and linkage as well as the modal damping of the spar structural modes must also be determined from experiments. A process for the estimating each of these terms is presented below.

A. Motor Drive Torque

The generalized force Q_{m_θ} is the motor drive torque, which is given by

$$Q_{m_\theta} = \frac{K_T}{R_a} e_a \quad (119)$$

The motor torque constant K_T and armature resistance R_a must be measured, or supplied by the motor manufacturer. A description of how to estimate the motor torque constant from experiments is provided below. The armature voltage e_a forms the external input into the equations of motion.

B. Generalized Frictional Force

The overall generalized friction force Q_{i_θ} is a lumped parameter that includes the effects of back-EMF and viscous friction in the gear train, linkage and the motor itself:

$$Q_{i_\theta} = B_\theta \dot{\theta} \quad (120)$$

where

$$B_\theta = -\left(\frac{K_T K_B}{R_m} + b\right) \quad (121)$$

A description of how the terms in Eq. (120) were measured follows.

1. Determination of Motor Characteristics

The important physical properties of most small motors being used in flapping-wing MAV prototypes are not well characterized by their manufacturer. This is because many of these motors are used to power toys or pager motors, and such detailed design information is not required for those applications. A method for extracting estimates of the required motor parameters is presented.

First, consider the problem of extracting of the back-EMF constant of the motor. By substituting Eq. (3) into Eq. (5), one can solve for K_b :

$$K_b = \frac{1}{\dot{\theta}} (e_a - R_a i_a) \quad (122)$$

Most of the parameters on the right-hand side of the equation are measurable in the laboratory using a digital multimeter. The measurement of $\dot{\theta}$ can be performed using a strobe light, an optical encoder, or a visual image correlation system. Alternatively, Eq. (3) can be used directly if an active drive motor is coupled to an optical encoder and to the test motor via an idler gear. The output voltage e_b generated by the test motor can be measured, while the period of the pulse train generated by the optical encoder can be used to determine the motor speed. Each of the methods described above have been used by the authors and have been found to produce nearly identical estimates of the back-EMF constant on a 7 mm pager motor manufactured by Super Slicks. The motor used in the test article is known in hobbyist circles as a Red Super Slicks motor and has an armature resistance of 2.3 Ω .

The estimation of the torque constant K_T followed the method outlined by the Didel company.** A pinion was mounted on the motor shaft. An arm with a splined hole near one end was fitted over the pinion. A point on the opposite end of the arm was oriented perpendicular to the longitudinal axis of the arm. The motor was mounted securely to a laboratory bench and the point of the arm was placed on a scale with a 0.1 g resolution. Multiplying the moment arm by the force measurement yielded the stall torque. The torque constant was then determined from Eq. (2). The resulting mean estimate for the torque constant was 6774 dyne-cm/A with a standard deviation of 619 dyne-cm/A. The high standard deviation was attributed to the low resolution of the scale used in the test.

2. Determination of Mechanism Friction

An initial estimate of the friction characteristics of the mechanism was obtained by measuring the steady-state speed of the motor, gear train, and linkage and the current flowing through the motor. Note that the wing spar was not attached to the mechanism during this test. A viscous friction model was used to describe the effect of all sources of mechanical friction within the subsystem, viz.,

$$\tau_f = -b\dot{\theta} \quad (123)$$

With knowledge of the motor torque constant, back-EMF constant, steady-state current, and steady-state speed, the viscous friction coefficient was estimated from

$$b = \frac{-K_T i_a}{\dot{\theta}_{ss}} - \frac{K_T K_b}{R} \quad (124)$$

where $\dot{\theta}_{ss}$ represents the steady-state velocity of the motor. In the work presented here, the initial estimate of the viscous friction coefficient was obtained from experimental data from a mechanism-only test. The final adjustment of the coefficient was performed by comparing simulation time histories of crank speed to experimental measurements of crank speed using an optical encoder. It was found that the viscous friction coefficient that caused the spar stroke periods of the simulation to match those observed in the experiment was $b = 0.525$ dyne-cm/(rad/s). It should be noted that this parameter, is very sensitive to the method of construction of the overall device. For example, friction produced by the linkage rivets or pins is related to the skill of the builder, who must carefully deform the heads of the rivets to ensure planar motion of the linkage without producing excessive friction.

C. Determination of Modal Characteristics of the Spar

An estimate of the modal damping of a spar or wing structure is not normally available. A test was conducted to estimate the modal damping of the first bending mode the spar used in the experiment.

**Data available online at <http://www.didel.com/microkit/moteurs/Motors.html> [retrieved 8 July 2011].

The spar under consideration was a carbon-fiber rod that the manufacturer markets as an 0.037-in.-diam. rod. The rod was cut to 13 cm in length. An infrared noncontact proximity sensor, consisting of an LED and photo transistor, was used measure the deflection of a point on the spar, while the root was clamped. The spar was plucked and the response was recorded at a 20 kHz sampling rate. The damping was estimated by using the well-known logarithmic decrement technique. The undamped natural frequency was also estimated from the response. The magnitude of the initial tip displacement was purposely small, i.e., less than 1 cm, in order to minimize the impact of aerodynamic drag upon the damping estimate. The measurement of the spar displacement in this test was limited to sensor voltage output, since the measurement of frequency and damping is not dependent upon the actual physical units of displacement, e.g., centimeters.

Some important observations were made while conducting the test. First, commercially available carbon-fiber rod does not have a circular cross section. The cross section is best described as an oval, rather than a 0.037 in. rod with a circular cross section. The cross-sectional measurements varied by ± 0.002 in. (± 0.005 cm). This means that pluck tests must be conducted with care, since an initial deformation that is not aligned with a principal axis will produce transverse vibrations along two axes, making it difficult for a noncontacting proximity sensor to accurately measure the time history of the displacement, which is required for the application of the log decrement method. The best results were obtained when the initial deformation was aligned with a principal axis. The response, as measured by the noncontact proximity sensor, was bandpass-filtered with break frequencies two times lower and two times higher than the theoretical estimate of the first bending-mode frequency for a spar with a circular cross section. The power spectral density of the filtered response was used to estimate the actual first bending-mode frequency.

Classical beam theory estimates the natural frequency of the first bending mode of a cantilever beam to be given by Eq. (52). To estimate the frequency of the first bending mode of the spar from Eq. (52), one must use estimates of the following spar properties: Young's modulus, cross-sectional area moment of inertia, mass per unit length, and length. The mass of the spar was determined to the nearest 1 mg on a precision scale and the length of the rod was measured to the nearest 0.25 mm using a digital caliper. The mass per unit length of the spar was determined to be $\hat{m} = 0.01085$ g/cm. Using the above information and the manufacturer's specifications for $E_s = 1.227 \times 10^{12}$ dyne/cm², as well as the assumption that the cross section of the rod is circular, the idealized first bending-mode frequency can be computed to be $\omega_{1\text{theory}} = 432.88$ rad/s. Since the product $E_s I_s$ had a higher degree of uncertainty than the spar mass and length, the measured first bending-mode frequency obtained from the peak of the power spectral density was used to estimate the uncertain product. The power spectral density of the bandpass-filtered tip deflection time history showed that the natural frequency of the first bending mode was located at 422.79 rad/s. For a uniform circular cross section of an 0.037 in. (0.09398 cm) round rod with an area moment of inertia about the neutral axis of $I_s = 3.83 \times 10^{-6}$ cm⁴, the value of Young's modulus that matches the observed

natural frequency is given by $E_s = 1.1704 \times 10^{12}$ dyne/cm², which is slightly lower than the manufacturer's specification. The lower frequency is most likely due to the departure from the ideal circular cross section of the rod. Indeed, beam theory predicts variations of up to $\pm 5\%$ in first bending-mode frequency for a rod with an elliptical cross section where the major and minor axes vary by ± 0.005 cm from a nominal 0.09398-cm-diam (0.037-in.-diam) circular cross section. The damping ratio for the first bending mode based upon the analysis using the log decrement method was found to be $\zeta_1 = 0.0025$; the damping ratio for the second bending mode was assumed to be the same as for the first.

D. Aerodynamic Drag Forces

The standard definition for the generalized forces used in Lagrange's equations is given by [29]

$$Q_i = \sum_{j=1}^n F_j \frac{\partial x_j}{\partial q_i} \quad (125)$$

where Q_i is the i th generalized force, F_j is the j th component of the external force applied to the system, q_i is the i th generalized coordinate, and $\partial x_j / \partial q_i$ is the j th component of the partial derivative of the position vector to the point of application of the force with respect to the i th generalized coordinate. For the derivation of the generalized forces acting on the flexible spar, the differential contribution to the generalized forces is first calculated. Then the differential contributions to the generalized forces are integrated to obtain generalized forces as a function of the angular position of the motor and the flexible modal coordinates. The derivation that follows assumes that the only external force applied to the system is due to the aerodynamic drag acting on the flexible spar and that the first two modal coordinates accurately represent the deformation. As shown in Fig. 5, the flexible spar is modeled as a cylinder and a blade-element model is used to determine the aerodynamic drag. As standard when using the blade-element method, the drag over the cylinder is modeled using a rectangle with dimensions equal to the cylinder's length and diameter. Thus, the replacement area lies in the \hat{s}_1 - \hat{s}_3 plane. Blade-element theory states [30]

$$dF_D = \frac{1}{2} \rho C_d V_\infty^2 dA \quad (126)$$

where V_∞ is the magnitude of the velocity of a point on the representative area once it has been resolved into components that lie in the plane of the blade element. dA is the differential area over which the dynamic pressure acts. Thus, $dA = dr_u dz_s$. It is convenient to describe the aerodynamic force in a frame that defines the blade elements. The definition of each blade element along the spar should remain constant in the coordinate frames in which they are expressed. Thus, at each point in the representative area a frame can be defined that deforms along with the spar. This deformed frame is related to the frame associated with the undeformed motion of the spar through a single axis rotation. The deformation of the spar is described in Eq. (45). The angle that defines the relationship between the s frame

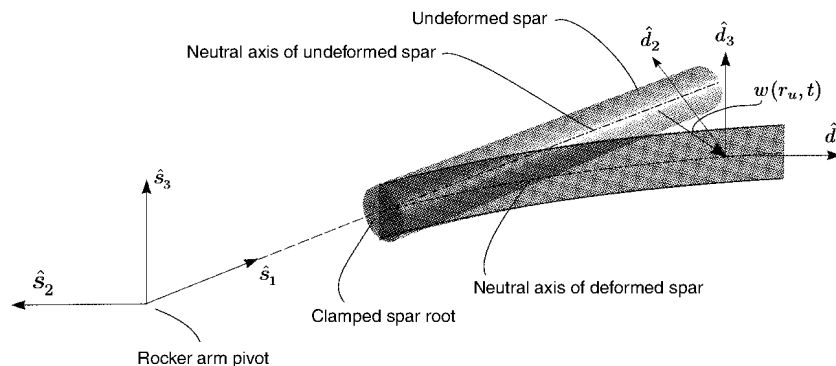


Fig. 5 Coordinate frames associated with undeformed and deformed spar.

and the deformed d frame is described by taking the spatial derivative of Eq. (45) with respect to the r_u variable. Thus,

$$w'(r_u, t) = \sum_{i=1}^{\infty} \Phi'_i(r_u) \eta_i(t) \quad (127)$$

As the present analysis assumes that only two modes are retained:

$$w'(r_u, t) = \Phi'_1(r_u) \eta_1(t) + \Phi'_2(r_u) \eta_2(t) \quad (128)$$

$$\begin{Bmatrix} \hat{s}_1 \\ \hat{s}_2 \\ \hat{s}_3 \end{Bmatrix} = \begin{bmatrix} \cos w'(r_u, t) & -\sin w'(r_u, t) & 0 \\ \sin w'(r_u, t) & \cos w'(r_u, t) & 0 \\ 0 & 0 & 1 \end{bmatrix} \begin{Bmatrix} \hat{d}_1 \\ \hat{d}_2 \\ \hat{d}_3 \end{Bmatrix} \quad (129)$$

The drag force acts in opposition to the direction of the velocity defined in the plane of the blade element. Thus, the differential force vector is written in the inertial frame as

$$d\mathbf{F}_d = \frac{1}{2} \rho C_d V_{\infty}^2 dA \left(-\frac{\mathbf{V}_{\infty}}{\|\mathbf{V}_{\infty}\|} \right) = \frac{1}{2} \rho C_d V_{\infty} (-\mathbf{V}_{\infty}) dA \quad (130)$$

To define \mathbf{V}_{∞} , begin with the definition of the velocity of the point written in terms of the deformed frame:

$$\begin{aligned} \mathbf{v}_{pr}^d &= [-(\Phi_1(r_u) \eta_1(t) + \Phi_2(r_u) \eta_2(t)) \dot{\phi}_l \cos w'(r_u, t) \\ &+ r \dot{\phi} \sin w'(r_u, t) + (\Phi_1(r_u) \dot{\eta}_1(t) \\ &+ \Phi_2(r_u) \dot{\eta}_2(t)) \sin w'(r_u, t)] \hat{d}_1 + [(\Phi_1(r_u) \eta_1(t) \\ &+ \Phi_2(r_u) \eta_2(t)) \dot{\phi}_l \sin w'(r_u, t) + r \dot{\phi} \cos w'(r_u, t) \\ &+ (\Phi_1(r_u) \dot{\eta}_1(t) + \Phi_2(r_u) \dot{\eta}_2(t)) \cos w'(r_u, t)] \hat{d}_2 \end{aligned} \quad (131)$$

As the blade element lies in the \hat{d}_2 - \hat{d}_3 plane, \mathbf{V}_{∞}^d is defined by ignoring the \hat{d}_1 component of \mathbf{v}_{pr}^d . Defining V_{∞} as the \hat{d}_2 component of \mathbf{V}_{∞}^d and writing the resulting vector in the inertial frame yields

$$\begin{aligned} \mathbf{V}_{\infty} &= (-\cos \phi_l \sin w'(r_u, t) - \sin \phi_l \cos w'(r_u, t)) V_{\infty} \hat{n}_1 \\ &+ (-\sin \phi_l \sin w'(r_u, t) + \cos \phi_l \cos w'(r_u, t)) V_{\infty} \hat{n}_2 \end{aligned} \quad (132)$$

The position vector to any point on the rectangle representing the spar can be written as

$$\begin{aligned} \mathbf{r}_{pr} &= (-r_r \cos \phi_l - r_u \cos \phi_l - \sin \phi_l \Phi_1 \eta_1 - \sin \phi_l \Phi_2 \eta_2) \hat{n}_1 \\ &+ (r_r \sin \phi_l + r_u \sin \phi_l + \cos \phi_l \Phi_1 \eta_1 + \cos \phi_l \Phi_2 \eta_2) \hat{n}_2 + z \hat{n}_3 \end{aligned} \quad (133)$$

From Eqs. (130) and (133) it is shown that both the differential force and the position vector from the origin to the point of application of the differential force are not explicit functions of the generalized coordinate θ ; however, recall that ϕ_l is a function of θ . Thus, the chain rule for partial derivation must be used in the determination of the differential contribution to the generalized force associated with the motor angular position. Thus,

$$dQ_{d_{\theta}} = dF_{Dx} \frac{\partial r_{prx}}{\partial \phi_l} \frac{\partial \phi_l}{\partial \theta} + dF_{Dy} \frac{\partial r_{pry}}{\partial \phi_l} \frac{\partial \phi_l}{\partial \theta} \quad (134)$$

$$dQ_{d_{\eta_1}} = dF_{Dx} \frac{\partial r_{prx}}{\partial \eta_1} + dF_{Dy} \frac{\partial r_{pry}}{\partial \eta_1} \quad (135)$$

$$dQ_{d_{\eta_2}} = dF_{Dx} \frac{\partial r_{prx}}{\partial \eta_2} + dF_{Dy} \frac{\partial r_{pry}}{\partial \eta_2} \quad (136)$$

Table 1 Parameters for the motor, gears, and encoders

Descriptions	Variables	Values	Units
Stage 1 gear ratio	G_1	9/48	—
Stage 2 gear ratio	G_2	12/81	—
Inertia of stage 1 gear	I_{G_1}	0.032334	g-cm ²
Inertia of stage 2 gear	I_{G_2}	0.25515	g-cm ²
Inertia of encoder	I_e	0.35329	g-cm ²
Inertia of 9-tooth pinion	I_{p9}	0.00013719	g-cm ²
Inertia of 12-tooth pinion	I_{p12}	0.0076397	g-cm ²
Inertia of motor armature	I_a	0.015845	g-cm ²
Motor torque constant	K_T	6774	(dyne-cm)/A
Motor back-EMF constant	K_b	0.000764	V/(rad/s)
Mechanism friction coefficient	b	0.525	dyne-cm/(rad/s)
Motor resistance	R_a	2.3	Ω

Table 2 Parameters for the four-bar linkage

Descriptions	Variables	Values	Units
Line-of-centers length	l_0	-1.936	cm
Crank length (link 1 formed by 81-tooth gear)	l_1	0.461	cm
Link 2 pin-to-pin length	l_2	2.060	cm
Link 3 pin-to-pin length	l_3	0.670	cm
Distance to c.g. of link 2 from connection point at link 1	l_{c2}	$\frac{1}{2} l_2$	cm
Distance to c.g. of link 3 from connection point at link 2	l_{c3}	0.753	cm
Distance to root of spar from rocker pivot	r_r	1.735	cm
Mass of pins at linkage joints	m_p	0.025	g
Mass of link 2	m_2	0.1072	g
Mass of link 3	m_3	0.1513	g
Moment of inertia of link 2 about its c.g.	I_2	0.06165	g-cm ²
Moment of inertia of link 3 about its c.g.	I_3	0.04283	g-cm ²

Table 3 Parameters for the flexible wing spar

Descriptions	Variables	Values	Units
Spar length	L	13.0	cm
Young's modulus of spar	E_s	1.1704×10^{12}	dyne/cm ²
Diameter of spar	d_s	0.0940	cm
Area moment of inertia of spar about neutral axis	I_s	3.8292×10^{-6}	cm ⁴
Mass per unit length of spar	\hat{m}	0.01085	g/cm
Length of spar adjoining rocker arm	l_r	0.556	cm
Modal damping ratio	$\zeta_1 = \zeta_2$	0.025	—

Thus,

$$Q_{d_\theta} = \int_0^L \left(dF_{Dx} \frac{\partial r_{pr_x}}{\partial \phi_1} \frac{\partial \phi_1}{\partial \theta} + dF_{Dy} \frac{\partial r_{pr_y}}{\partial \phi_1} \frac{\partial \phi_1}{\partial \theta} \right) \quad (137)$$

$$Q_{d_{\eta_1}} = \int_0^L \left(dF_{Dx} \frac{\partial r_{pr_x}}{\partial \eta_1} + dF_{Dy} \frac{\partial r_{pr_y}}{\partial \eta_1} \right) \quad (138)$$

$$Q_{d_{\eta_2}} = \int_0^L \left(dF_{Dx} \frac{\partial r_{pr_x}}{\partial \eta_2} + dF_{Dy} \frac{\partial r_{pr_y}}{\partial \eta_2} \right) \quad (139)$$

Note that these generalized forces are state-dependent; therefore, these spatial integrals must be evaluated at each simulation time step by quadrature.

E. Summary of Measured Parameters

Table 1 shows the estimates of the parameters of associated with the drive train elements. The inertias of the gears were estimated by weighing each gear on a precision scale to the nearest 0.1 mg. The gears were constructed in a 3-D CAD program and mass moment of inertia properties were estimated using the mass measurement and the computed volume to obtain the density of the material. The inertia of the coreless motor armature was estimated by dissection and measurement. The inside and outside diameter of the copper windings were measured, clipped off, and weighed on a scale to the nearest 0.1 mg. Similarly the spindle was measured and weighed separately. The armature assembly was drawn in a 3-D CAD program and the mass properties were estimated. It is important to accurately characterize the armature inertia because there is no mechanical advantage at the motor stage to mitigate its effect.

Table 2 shows the estimates of the parameters of associated with the drive train elements. These estimates were obtained by weighing the linkage elements on a scale to the nearest 0.1 mg and drawing the elements in a 3-D CAD package that provides mass property estimates.

Table 3 summarizes the parameter estimates associated with the wing spar.

VI. Results

A. Experiment

A bench-test experiment was performed using the mechanism shown in Fig. 1 for the purpose of providing a point of comparison for the simulation results. Four time-based measurements were acquired from the experiment: namely, the velocity of the first stage gear via an optical encoder, armature voltage, motor current, and digital images from a high-speed camera. Motor voltage, current, and encoder circuit waveforms were recorded by a data acquisition system.

An optical encoder with 16 slots ran at the same speed as the first stage gear, which rotated at 3/16 of the speed of the motor and 27/4 times faster than the speed of the crank gear. This arrangement yielded a resolution of 108 pulses per crank revolution and 3.357 pulses per motor revolution. The time delay between encoder pulses was measured by a 20 MHz clock within the data acquisition system. The pulse periods were measured from falling edge to falling edge. The detection of falling-edge pulses also triggered A/D sampling of the instantaneous armature voltage and supply current. A 2000

frame/second camera system captured overhead images of the system against the background of a protractor plate that was centered on the rocker-arm pivot. Protractor measurements for the spar tip could be read to the nearest 1/2° at low tip velocities; however, the spar appeared blurred over arcs of up to 3° at high tip velocities. Precise measurements of deflection were therefore only taken at the stroke-reversal points.

The experiment proceeded by triggering the camera system, applying 2.81 V from a regulated power supply to the motor armature, and recording a 4 s segment of the system response. The polarity of the voltage applied to the armature resulted in a clockwise crank rotation when viewed by the cameras, which is important to note because the system response is direction-dependent. The 4 s segment was sufficient for the system to achieve a long period of steady-state operation (defined as a condition where the period of crank rotation is constant from one wing beat cycle to the next). When synchronizing the camera clock to the data acquisition system clock, the first frame that motion was detected using the camera system was assumed to correspond to the first frame acquired by the data acquisition system. The accuracy of the time-base synchronization is therefore estimated to be within ± 0.0005 s.

B. Comparison of Simulation Results to Experimental Measurements

A segment of the simulation and experimental results for the system under steady-state operation is examined. Figure 6 shows a comparison of simulation time histories and experimental measurements that have been synchronized based upon extremal spar tip displacements. The experimental measurements that are presented here are typical of results that were observed over multiple experimental trials. The middle two displacement traces show the simulated time history of the angular displacement of the rocker arm (blue) and spar tip (green) as would be measured by the background protractor on the bench-test platform. The vertical red and blue lines indicate the times at which the extremal spar tip displacements were measured using the high-speed camera images. It can be seen that the period of the experimental results matches the period of the simulation results. This match was achieved by fine-tuning the friction coefficient b in the simulation until the crank rotation periods coincided, leaving all other parameters fixed at their measured or computed values. The measured values of the spar tip deflection at the extremal points were extracted from the camera images and appear as red and blue asterisks on the vertical lines associated with stroke reversals. Note that the spar tip deflections associated with the blue asterisks are greater than those associated with the red asterisks. This is because the linkage produces temporally asymmetric motion that results in a stronger reversal on one side than the other. This effect can be seen in the displacement plot as well, where the peaks associated with strong reversals are noticeably sharper than those associated with the weak reversals. The simulated tip deflections compare favorably with those measured by the camera at the extremal points. Finally, the experimentally measured and simulated crank frequencies can be seen in the top two traces. It can be seen that the characteristics of the time histories compare favorably. The simulation slightly underpredicts the peak experimental crank frequency of 14.85 Hz by predicting a value of 13.98 Hz for a difference of 4.9%. The simulation also slightly underpredicts the minimum experimental crank frequency of 11.03 Hz by predicting a value of 11.66 Hz for a difference of 5.7%.

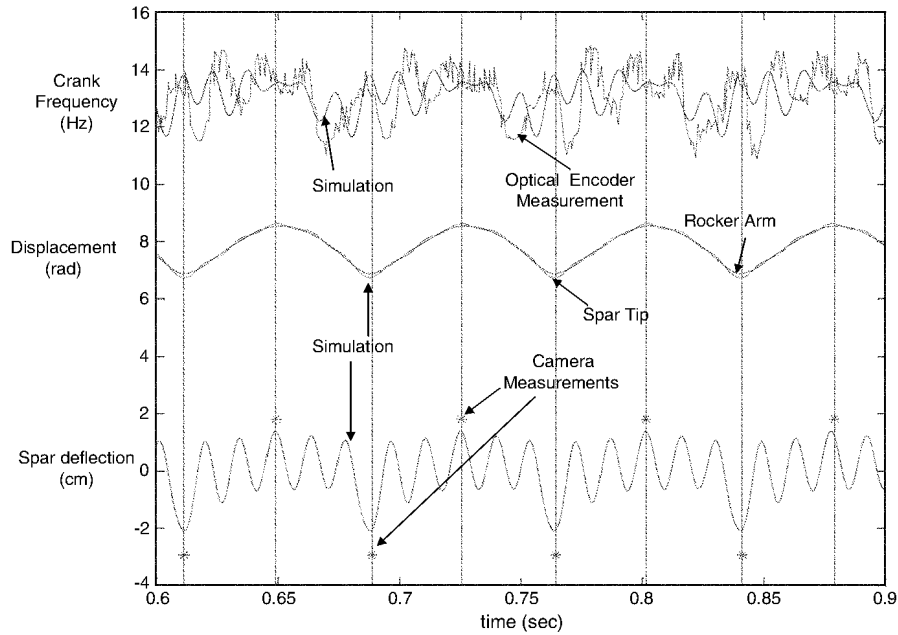


Fig. 6 Comparison of experimental and simulation results.

Another measure of the quality of the simulation is to compare multi-exposure images taken of the spar as it traverses from one reversal point to another. Figure 7 shows a comparison of enhanced camera images and the simulation images for the spar as it traverses from the weak to the strong reversal point for clockwise crank rotation. Reflections and blurred images obscure the spar in some segments of the motion; thus, the images have been enhanced by the use of a sketch overlay in order to improve the visibility of the spar. The sketched overlay was produced by carefully tracing over the centerline of each spar image with a solid black digital pen using image processing software. The images shown in Fig. 7 correspond

to the portion of the time histories between 0.802 and 0.841 s shown in Fig. 6. The most striking feature of the images is the dwell that occurs near the 60° mark. Another less significant dwell can be seen between 95° and 105°. This dwell effect is not readily discernible from time-history plots of state variables; however, the effect is a prominent feature of the motion that can be seen when viewing video images from the high-speed camera system. The appearance of the dwell phenomenon is a result of the combined motion of the flexible structure and the rocker arm. In the dwell regions, the spar is moving backward relative to the rocker arm as a result of dynamic structural deformation. Figure 8 shows a comparison of the enhanced camera

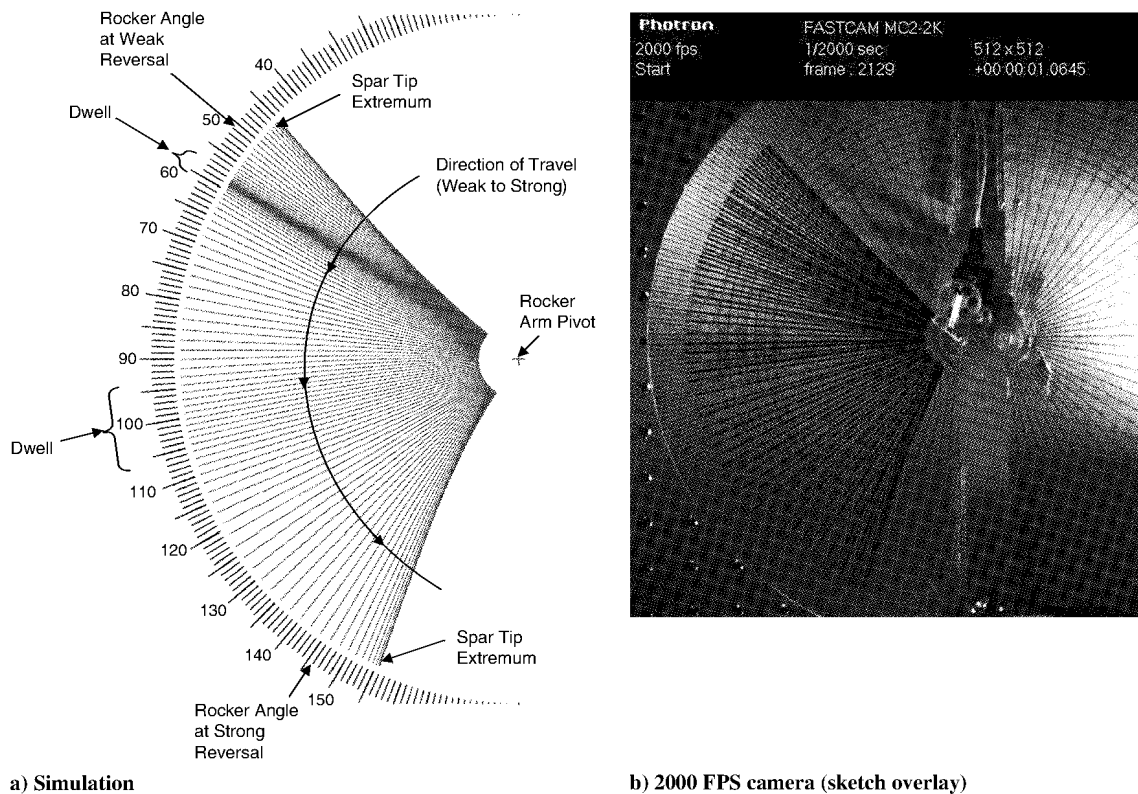


Fig. 7 Multi-exposure comparison on downstroke (weak to strong).

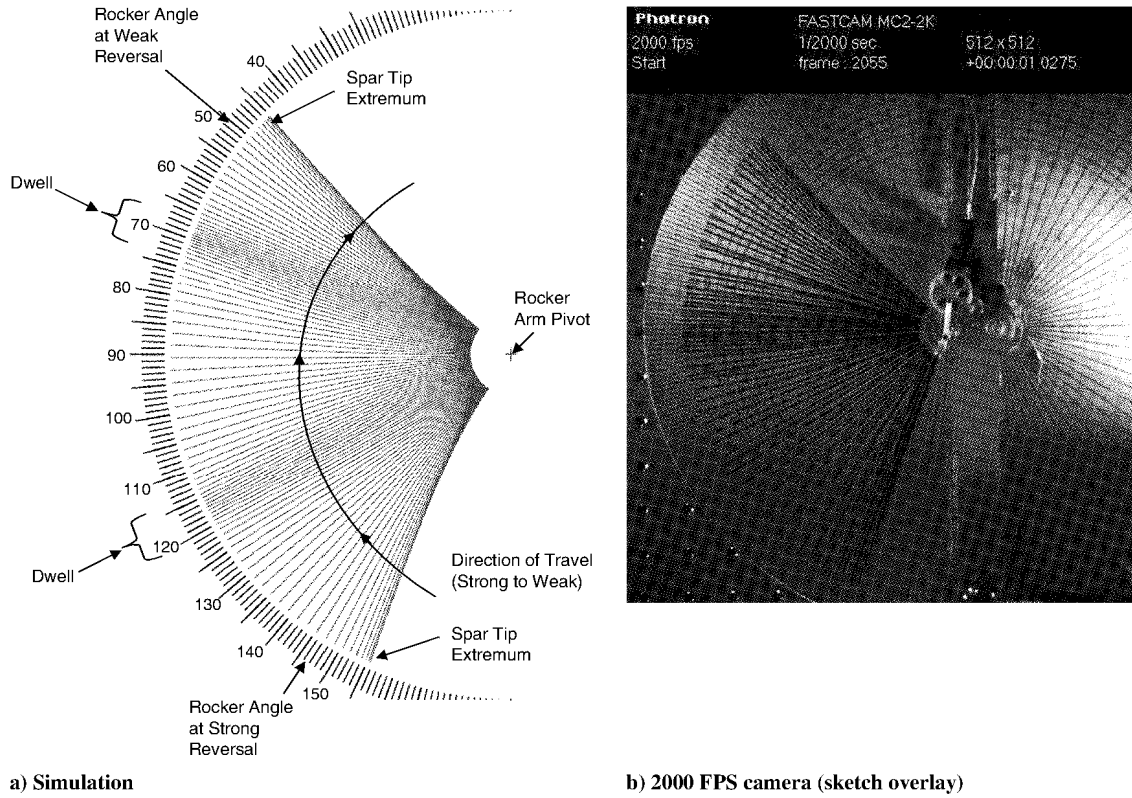


Fig. 8 Multi-exposure comparison on upstroke (strong to weak).

images and the simulation images for the spar as it traverses from the strong to the weak reversal point for clockwise crank rotation. The images correspond to the portion of the time histories between 0.841 and 0.879 s shown in Fig. 6. Two dwell regions can be seen in the simulation results, while one dwell region is noticeable in the camera images. The first dwell region in the simulation occurs in the 112 to

120° range, while the dwell region from the camera images occurs in the 90° range. It is not clear from the camera images that a second dwell occurs near the end of the stroke or whether the spar is simply slowing down near the reversal point. In any case, there appears to be some small phase differences in the time histories and in the multi-exposure spar images in this region. Clearly, the presence of such

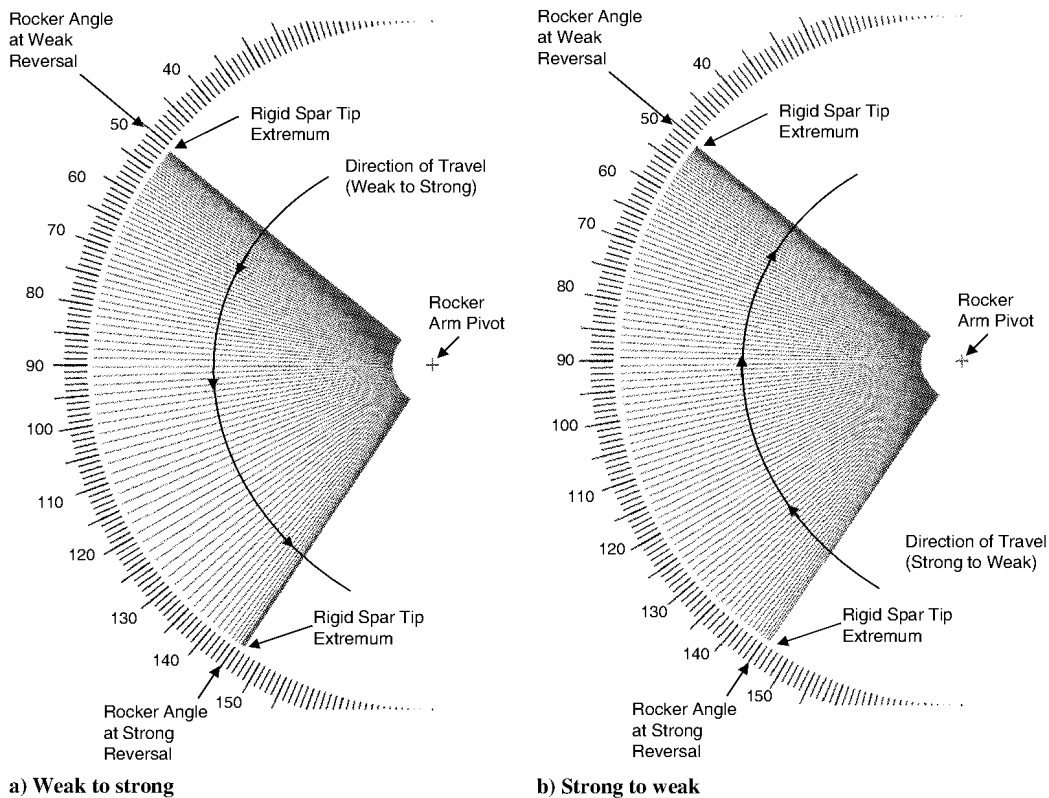


Fig. 9 Naive simulation, constant velocity motor, rigid spar.

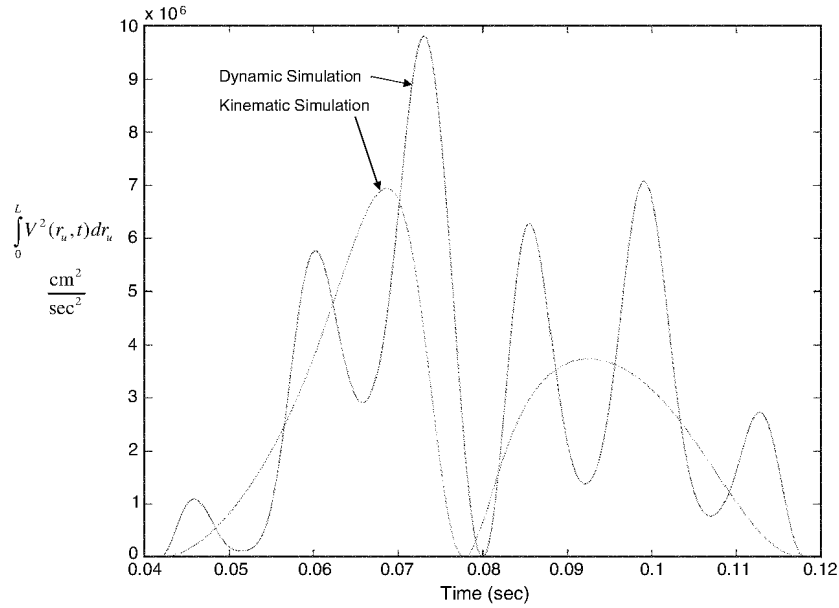


Fig. 10 Behavior of velocity squared integral, related to magnitude of aerodynamic forces.

dwel regions has a significant effect upon the local dynamic pressure experienced by the spar and the resulting aerodynamic loads.

The multi-exposure plot shown in Fig. 9 is the result of a naive simulation, where the motor maintains a constant velocity and the spar is rigid. The absence of midstroke dwell regions is clear. A more subtle, but important, point of comparison lies in the behavior of the motion near the reversal points. Close examination of the figures reveals that the motion near the reversal points with flexible dynamics is faster than that which occurs in the purely kinematic simulation. The dynamic motion of the spar near the endpoints could be colloquially described as having a whipping action. This whipping motion and the increase in stroke amplitude also affect the aerodynamic loads. The impact of the modeling error associated with the kinematic simulation on aerodynamic loads can be assessed by comparing the behavior of two time-varying integrals over the course of a wingbeat. The magnitude of an arbitrary aerodynamic load F created by a dynamic pressure distribution over the length of the spar is given by

$$F = \frac{1}{2} \rho C_F d_s \int_0^L V^2(r_u, t) dr_u \quad (140)$$

If over the course of a wingbeat, the terms premultiplying the velocity squared integral are taken to be constant, then the differences between the integrals for the kinematic simulation and the dynamic simulation are a measure of the differences in instantaneous aerodynamic force. For the full dynamic simulation,

$$\begin{aligned} \int_0^L V^2(r_u, t) dr_u = & c_1 S_2^2 \dot{\theta}^2 + c_2 (S_2^2 \dot{\theta}^2 \eta_1^2 + \dot{\eta}_1^2) + 2c_4 S_2 \dot{\theta} \dot{\eta}_1 \\ & + c_7 (S_2^2 \dot{\theta}^2 \eta_2^2 + \dot{\eta}_2^2) + 2c_8 S_2 \dot{\theta} \dot{\eta}_2 \end{aligned} \quad (141)$$

whereas for the kinematic simulation,

$$\int_0^L V_k^2(r_u, t) dr_u = c_1 S_2^2 \dot{\theta}^2 \quad (142)$$

A plot that compares the two integrals over the course of a wingbeat is shown in Fig. 10. It can be seen that the flexible dynamics significantly influence the value of this integral and, therefore, the magnitude of the aerodynamic loads. It was found that the cycle-averaged value of the integral from the dynamic simulation was $3.1659 \times 10^6 \text{ cm}^2/\text{s}^2$, while the value corresponding to the kinematic simulation results was $2.5511 \times 10^6 \text{ cm}^2/\text{s}^2$, which indicates that the aerodynamic loads produced by the flexible spar would be about 24% higher than those predicted by a simple kinematic

simulation. It can be concluded that despite fluctuations in the motor speed and the presence of dwell regions, the flexible spar produces higher average aerodynamic loads than the rigid spar. The higher loads are the result of an increase in effective stroke amplitude and velocity near the stroke-reversal points.

An additional observation was that the inclusion of the dynamics of the second bending mode, in this particular case, was not warranted. A short study was conducted in which all terms in Eq. (118) that were associated with the second bending mode were set to zero. The simulation results generated by the model that included the rigid-body coordinate and the first bending mode were visually indistinguishable from those shown in Figs. 6–8 and 10. Furthermore the change in the cycle-averaged value of the velocity squared integral occurred in the 4th decimal place, i.e., $3.1656 \times 10^6 \text{ cm}^2/\text{s}^2$ for the single mode versus $3.1659 \times 10^6 \text{ cm}^2/\text{s}^2$ for the second mode.

This work considers the dynamic coupling between ornithopter subsystems from the motor to the wing spar. To analyze a system that includes wing ribs and membrane elements, at least two additional degrees of freedom should be considered, viz., wing torsion and out-of-plane bending. An analysis that includes these additional wing elements is beyond the scope of the present paper and will be considered in future work.

VII. Conclusions

From the comparison of the simulation and experimental results, it is concluded that the Lagrangian analysis method captures the major features and trends observed in the experiment significantly better than constant velocity motor and rigid-spar kinematic simulations used by previous investigators. Furthermore, it is concluded that dynamic interactions between the flexible wing elements, drivetrain, and motor have a significant effect upon both the instantaneous and cycle-averaged aerodynamic loads upon the spar. Thus, when designing machines to optimize wing motion or attempting to match wing-stroke patterns observed in natural flyers, one must consider coupling between drive components and the wings rather than simply prescribing wing kinematics. The validation of the equations of motion by comparing simulation results to experimental measurements, instills confidence in the accuracy of the model. It was also found that in the specific case considered in the experiment, the second bending mode had little effect upon the model predictions. It is therefore expected that in many cases, it may be possible to ignore second bending-mode effects and still maintain an adequate level of accuracy. Although the model was validated on a single test bed, the modeling framework is applicable to a large class of MAV

ornithopters. The equations of motion presented in this paper can be used to predict how dc-motor-powered flapping-wing micro air vehicle (MAV) subsystem elements will behave when a constant or time-varying voltage is applied to the motor armature. These equations provide a powerful analysis tool for MAV system designers because they can be used as the basis for a systematic method of selecting motors, drivetrains, linkage kinematics, and designing structural and aerodynamic properties of flapping-wing MAVs. They also have the potential to support mechanism control law designs that can improve the behavior of wingbeat motion over what could be achieved by simply applying a constant voltage to the drive motor.

Appendix: Differentiation of the Configuration-Dependent Terms in the Four-Bar Linkage

To evaluate Eq. (101) the following relationships are required:

$$\frac{\partial S_1}{\partial \theta} = -\Gamma^2 \frac{l_1 \cos(\phi_l - \Gamma\theta)}{l_2 \sin(\alpha_l - \phi_l)} \quad (\text{A1})$$

$$\frac{\partial S_1}{\partial \alpha_l} = -\Gamma \frac{l_1 \cos(\alpha_l - \phi_l) \sin(\phi_l - \Gamma\theta)}{l_2 \sin^2(\alpha_l - \phi_l)} \quad (\text{A2})$$

$$\frac{\partial S_1}{\partial \phi_l} = \Gamma \frac{l_1 \sin(\alpha_l - \Gamma\theta)}{l_2 \sin^2(\alpha_l - \phi_l)} \quad (\text{A3})$$

$$\frac{\partial S_2}{\partial \theta} = -\Gamma^2 \frac{l_1 \cos(\alpha_l - \Gamma\theta)}{l_3 \sin(\alpha_l - \phi_l)} \quad (\text{A4})$$

$$\frac{\partial S_2}{\partial \alpha_l} = -\Gamma \frac{l_1 \sin(\phi_l - \Gamma\theta)}{l_3 \sin^2(\alpha_l - \phi_l)} \quad (\text{A5})$$

$$\frac{\partial S_2}{\partial \phi_l} = \Gamma \frac{l_1 \sin(\alpha_l - \Gamma\theta) \cos(\alpha_l - \phi_l)}{l_3 \sin^2(\alpha_l - \phi_l)} \quad (\text{A6})$$

$$\frac{\partial C_1}{\partial \theta} = -\Gamma \sin(\Gamma\theta - \alpha_l) \quad (\text{A7})$$

$$\frac{\partial C_1}{\partial \alpha_l} = \sin(\Gamma\theta - \alpha_l) \quad (\text{A8})$$

Acknowledgments

The authors would like to recognize the efforts of Benjamin Perseghetti, Kyle Carson, and 1st Lt. Eric Wolf for their support in the construction of the test article and for taking measurements of vehicle components. Michael Porter from Data Science Automation is acknowledged for the design and construction of the optical encoder, the noncontact proximity sensor, and for programming the LabVIEW Virtual Instruments that made it possible to record the experimental data. The experimental research was conducted in the U.S. Air Force Research Laboratory Micro Air Vehicle Integration and Application Research Institute facility at Wright-Patterson Air Force Base, Ohio. The overall research project was supported under a laboratory task administered by the U.S. Air Force Office of Scientific Research (Fariba Fahroo, Program Manager).

References

- [1] Weis-Fogh, T., and Jensen, M., "Biology and Physics of Locust Flight, I: Basic Principles in Insect Flight. A Critical Review," *Proceedings of the Royal Society of London, Series B: Biological Sciences*, Vol. 239, No. 667, 1956, pp. 415–458.
- [2] Ellington, C. P., "The Aerodynamics of Hovering Insect Flight, Parts I–VI," *Proceedings of the Royal Society of London, Series B: Biological Sciences*, Vol. B305, No. 4, 1984, pp. 1–181.
- [3] Thomas, A. L. R., and Taylor, G. K., "Animal Flight Dynamics I. Stability in Gliding Flight," *Journal of Theoretical Biology*, Vol. 212, No. 3, 2001, pp. 399–424. doi:10.1006/jtbi.2001.2387
- [4] Taylor, G. K. and Thomas, A. L. R., "Animal Flight Dynamics II. Longitudinal Stability in Flapping Flight," *Journal of Theoretical Biology*, Vol. 214, No. 3, 2002, pp. 351–370. doi:10.1006/jtbi.2001.2470
- [5] Shyy, W., Lian, Y., Tanj, J., Viieru, D., and Liu, H., *Aerodynamics of Low Reynolds Number Flyers*, Cambridge Univ. Press, New York, 2008, pp. 1–27.
- [6] de Croon, G. C. H. H., de Clercq, K. M. E., Ruijsink, R., Remes, B., and de Wagter, C., "Design, Aerodynamics, and Vision-Based Control of the DelFly," *International Journal of Micro Air Vehicles*, Vol. 1, No. 2, June 2009, pp. 71–97. doi:10.1260/175682909789498288
- [7] Jones, K. D., Bradshaw, C. J., Papadopoulos, J., and Platzer, M. F., "Bio-Inspired Design of Flapping-Wing Micro Air Vehicles," *The Aeronautical Journal*, Vol. 109, No. 1098, Aug. 2005, pp. 385–393.
- [8] Gerdes, J. W., Gupta, S. K., and Wilkerson, S. A., "A Review of Bird-Inspired Flapping Wing Miniature Air Vehicle Designs," *Proceedings of the ASME Design Engineering and Technical Conferences*, DETC Paper No. 2010-28513, Montreal, Aug. 2010, pp. 57–67.
- [9] Doman, D. B., and Regisford, S., "Wing Sizing, Trim, and Control Consideration in the Design of Hover Capable Flapping Wing Micro Air Vehicles," AIAA Paper 2010-7629, Aug. 2010.
- [10] Madangopal, R., Khan, Z. A., and Agrawal, S. K., "Energetics-Based Design of Small Flapping-Wing Micro Air Vehicles," *IEEE/ASME Transactions on Mechatronics*, Vol. 11, No. 4, Aug. 2006, pp. 433–438. doi:10.1109/TMECH.2006.878525
- [11] McDonald, M., and Agrawal, S. K., "Design of a Bio-Inspired Spherical Four-Bar Mechanism for Flapping-Wing Micro-Air-Vehicle Applications," *Journal of Mechanisms and Robotics*, Vol. 2, No. 2, May 2010, Paper 021012. doi:10.1115/1.4001460
- [12] Rehmat, Z., Roll, J., Lee, J. S., Yim, W., and Trabia, M. B., "Design of 'Figure-8' Spherical Motion Flapping Wing for Miniature UAV," *Proceedings of the ASME Design Engineering and Technical Conferences*, San Diego, CA, Aug.–Sept. 2009, pp. 539–546.
- [13] Trabia, M. B., Yim, W., Rehmat, Z., and Roll, J., "Flight Characteristics of Flapping Wing Miniature Air Vehicles with 'Figure-8' Spherical Motion," *Proceedings of the ASME International Mechanical Engineering Congress and Exposition*, Buena Vista, FL, Nov. 2009, pp. 293–300.
- [14] Raney, D. L., and Slominski, E. C., "Mechanization and Control Concepts for Biologically Inspired Micro Air Vehicles," *Journal of Aircraft*, Vol. 41, No. 6, 2004, pp. 1257–1265. doi:10.2514/1.5514
- [15] Chung, S. J., Stoner, J. R., and Dorothy, M., "Neurobiologically Inspired Control of Engineered Flapping Flight," AIAA Paper 2009-1929, April 2009.
- [16] Berman, G., and Wang, Z., "Energy-Minimizing Kinematics in Hovering Insect Flight," *Journal of Fluid Mechanics*, Vol. 582, 2007, pp. 153–168. doi:10.1017/S0022112007006209
- [17] Kurdi, M., Stanford, B., and Beran, P., "Kinematic Optimization of Insect Flight for Minimum Mechanical Power," AIAA Paper 2010-1420, Jan. 2010.
- [18] Soueid, H., Guglielmini, L., Airiau, C., and Bottaro, A., "Optimization of the Motion of a Flapping Airfoil Using Sensitivity Functions," *Computers and Fluids*, Vol. 38, No. 4, 2009, pp. 861–874. doi:10.1016/j.compfluid.2008.09.012
- [19] Deng, X., Schenato, L., Wu, W. C., and Sastry, S. S., "Flapping Flight for Biomimetic Robotic Insects: Part I—System Modeling," *IEEE Transactions on Robotics and Automation*, Vol. 22, No. 4, Aug. 2006, pp. 776–788.
- [20] Deng, X., Schenato, L., and Sastry, S. S., "Flapping Flight for Biomimetic Robotic Insects: Part II—Flight Control Design," *IEEE Transactions on Robotics and Automation*, Vol. 22, No. 4, Aug. 2006, pp. 789–803.
- [21] Khan, Z. A., and Agrawal, S. K., "Control of Longitudinal Flight Dynamics of a Flapping-Wing Micro Air Vehicle Using Time-Averaged Model and Differential Flatness Based Controller," *Proceedings of the American Control Conference*, IEEE, New York, Jul. 2007, pp. 5284–5289.
- [22] Dileo, C., and Deng, X., "Design of and Experiments on a Dragonfly-Inspired Robot," *Advanced Robotics*, Vol. 23, Nos. 7–8, 2009, pp. 1003–1021. doi:10.1163/156855309X443160
- [23] Wood, R. J., Avadhanula, S. M., and Fearing, R. S., "Microrobotics using Composite Materials: The Micromechanical Flying Insect

- Thorax," *Proceedings of the IEEE International Conference on Robotics and Automation*, Vol. 2, IEEE Press, Piscataway, NJ, 2003, pp. 1842–1849.
- [24] Wood, R., "The First Takeoff of a Biologically Inspired At-Scale Robotic Insect," *IEEE Transactions on Robotics and Automation*, Vol. 24, No. 2, 2007, pp. 341–347.
- [25] Avadhanula, S., Wood, R., Campolo, D., and Fearing, R., "Dynamically Tuned Design of the MFI Thorax," *IEEE International Conference on Robotics and Automation*, Vol. 1, IEEE Press, Piscataway, NJ, May 2002, pp. 52–59.
- [26] Ogata, K., *Modern Control Engineering*, 2nd ed., Prentice-Hall, Englewood Cliffs, NJ, 1990, pp. 118–122.
- [27] Meirovitch, L., *Analytical Methods in Vibrations*, Macmillan, New York, 1967, pp. 161–166, 233–235.
- [28] Craig, R. R., *Fundamentals of Structural Dynamics*, Wiley, Hoboken, NJ., 2006, p. 35.
- [29] Greenwood, D. T., *Principles of Dynamics*, 2nd ed., Prentice-Hall, Upper Saddle River, NJ, 1988, pp. 259–262.
- [30] Osborne, M., "Aerodynamics of Flapping Flight with Application to Insects," *Journal of Experimental Biology*, Vol. 28, pp. 221–245.